Fig. 4.2: (a) Photoluminescence spectra of PVK:Bu-PPyV blend thin films with different Bu-PPyV content. The excitation wavelength was 420 nm, exciting only Bu-PPyV chromophores. (b) Relative integrated PL efficiency of Bu-PPyV chromophores vs. Bu-PPyV content in the PVK:Bu-PPyV or PVK:PBD:Bu-PPyV blend thin films. The strengths were normalized by the strength of the absorption at 420 nm in each film.

broadened and shifts to the red. The same evolution of PL was observed for the PVK:PBD:Bu-PPyV three-component system. By normalizing the integrated PL intensity with the absorption of the same blend film at 420 nm, the relative PL efficiencies of Bu-PPyV chromophores blended in PVK or PVK:PBD are obtained and displayed in Fig. 4.2(b). The Bu-PPyV chromophores at low concentration are found to be over one order of magnitude more efficient than those in pure Bu-PPyV films or those at high concentration. A similar concentration-dependent luminescence of Bu-PPyV is also observed in its solutions in organic solvents [1,2], as shown in Fig. 4.3. This precludes the possibility that the emission is from a complex between Bu-PPyV and PVK or PBD in the excited state, such as a charge-transfer exciplex, which can also lead to a shift of emission towards lower energies as well as a decrease in luminescence efficiency. The strong dependence of luminescence on the chromophore concentration in both solvents and solid solutions (i.e. blends) clearly suggests that the transition is from the emission of isolated chromophores to the emission of excimers. The efficient green PL in both dilute solutions and blends with low Bu-PPyV contents is therefore assigned to the emission of isolated Bu-PPyV chromophores, while the weak red PL in blends with high Bu-PPyV contents and pure Bu-PPyV thin films is attributed to Bu-PPyV excimer emission. Bu-PPyV excimers form probably due to the strong interaction between Bu-PPyV chromophores at higher concentrations. The PL efficiency starts dropping rapidly around 2 wt.% Bu-PPyV. It is clear that blending Bu-PPyV with the high energy-gap PVK eliminates the interaction between Bu-PPyV chromophores and maintains the high PL efficiency of isolated Bu-PPyV chromophores in the solid state. All these luminescent properties strongly suggest that the Bu-PPyV and PVK chains are homogeneously mixed to the molecular level, and that PVK has actually "diluted" Bu-PPyV chromophores like the solvents do. This is consistent with the TEM of I_2-stained PVK:Bu-PPyV blend films floated off the substrate. Fig. 4.4 shows the TEM of a stained 1000-Å-thick free-standing PVK:Bu-PPyV (100:5) blend thin film on top of a porous carbon film, revealing no phase
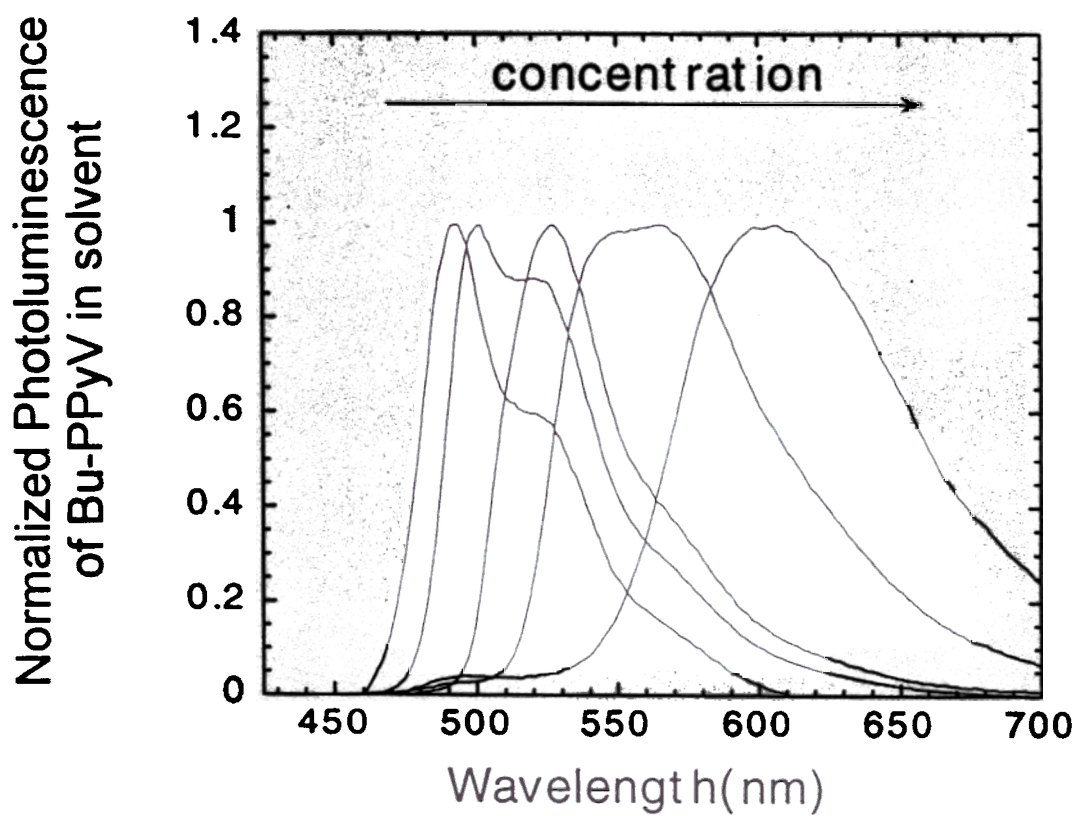
Fig. 4.3: Photoluminescence spectra of Bu-PPyV in THF at concentrations (from left to right) of 2×10^{-6}, 2×10^{-4}, 2×10^{-3}, 2×10^{-2}, and 0.1 M (concentration based on monomer unit). (from Ref. [2])
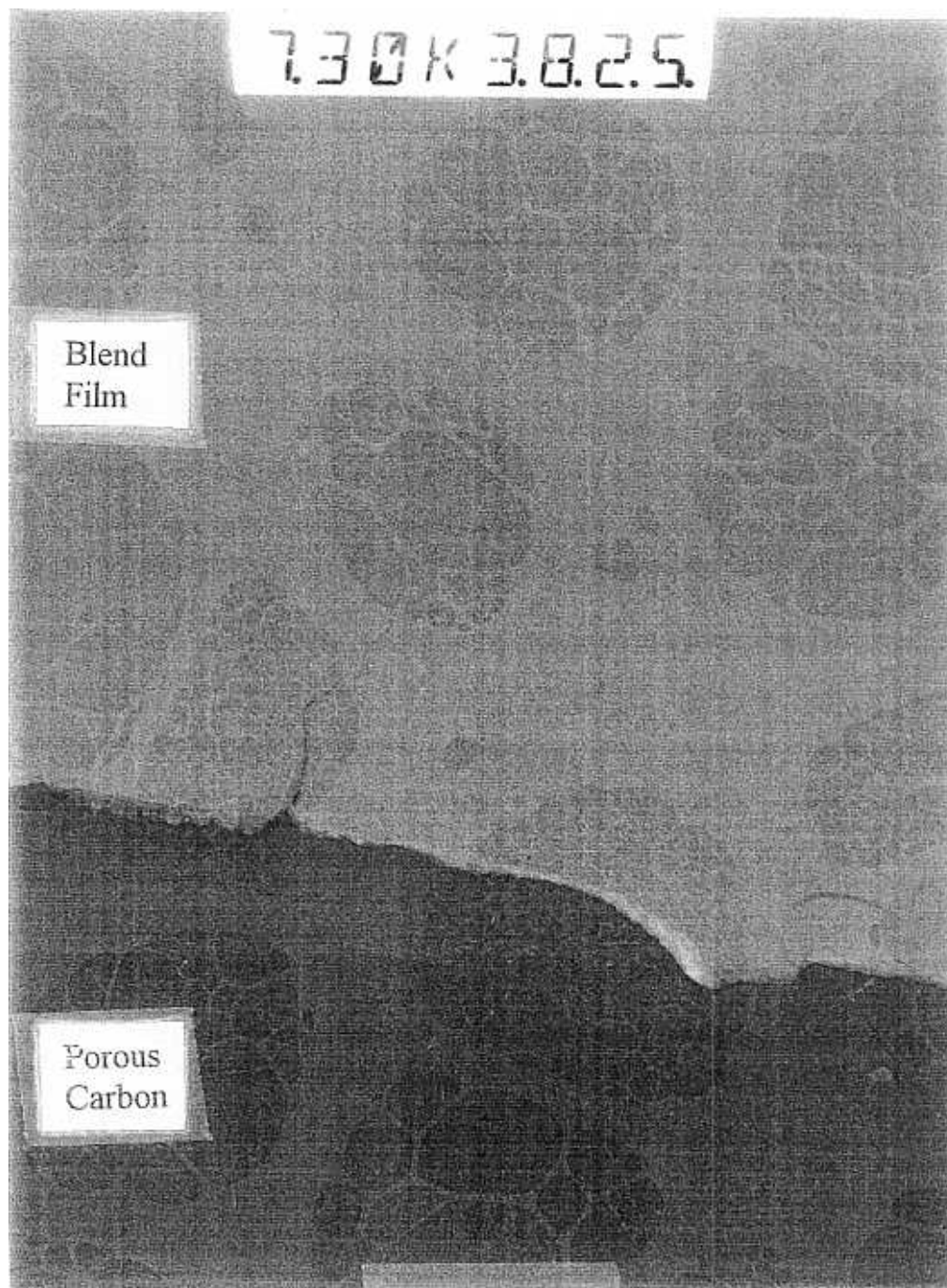
Fig. 4. TEM the I$_2$-stained PVK:Bu-PPy**V** (100: wt. blend thin film top the porous carbon film.

separation between Bu-PPyV and PVK in the as-spun films. It is also seen in the TEM that the spin-coated blend thin film has an uniform appearance.

With the excitation wavelength at 420 nm, excitons are formed only on Bu-PPyV chromophores, so the emission behavior of the Bu-PPyV chromophore itself in PVK or PVK:PBD matrix is investigated. On the other hand, by exciting into the absorption range of higher energy gap PVK and PBD using the 340 nm excitation, energy transfer between materials is probed. Fig. 4.5(a) plots the PL spectra of various PVK:Bu-PPyV blends using 340 nm excitation. With the Bu-PPyV content as low as 1 wt.%, almost all emission is from Bu-PPyV even though almost all excitation energy is absorbed by PVK. The emission from other components can only coexist with Bu-PPyV emission at extremely low Bu-PPyV content. A similar transition in emission was also observed between PVK:PBD and Bu-PPyV in the PVK:PBD:Bu-PPyV blends. Therefore we can conclude that excitons formed in PVK or PVK:PBD of the blends efficiently transfer to Bu-PPyV chromophores. Such a transfer could happen through the radiative transfer process, the Förster transfer process or the exciton transfer (migration) process, since Bu-PPyV has a lower energy gap than both PVK and PBD and the emission spectrum of PVK or PBD matches the absorption spectrum of Bu-PPyV fairly well. By normalizing the integrated PL intensity with the absorption of the same blend film at 340 nm, the relative PL efficiency as a function of Bu-PPyV concentration is displayed in Fig. 4.5(b). For both PVK:Bu-PPyV and PVK:PBD:Bu-PPyV systems, there is modest enhancement of PL using 340 nm excitation in comparison with the PVK or PVK:PBD host without Bu-PPyV chromophores, by a factor of roughly two around -2 wt.% Bu-PPyV , indicating the small amount of Bu-PPyV doped into the PVK or PVK:PBD provides a more efficient radiative recombination channel for excitons. The gain in the luminescence efficiency in a guest-host system usually requires: (i) a high luminescence yield of the emitting dopants when excitons form on them, (ii) efficient energy transfer from the host to emitting dopants, and (iii) a shorter lifetime of the excited states (or excitons) of the emitting
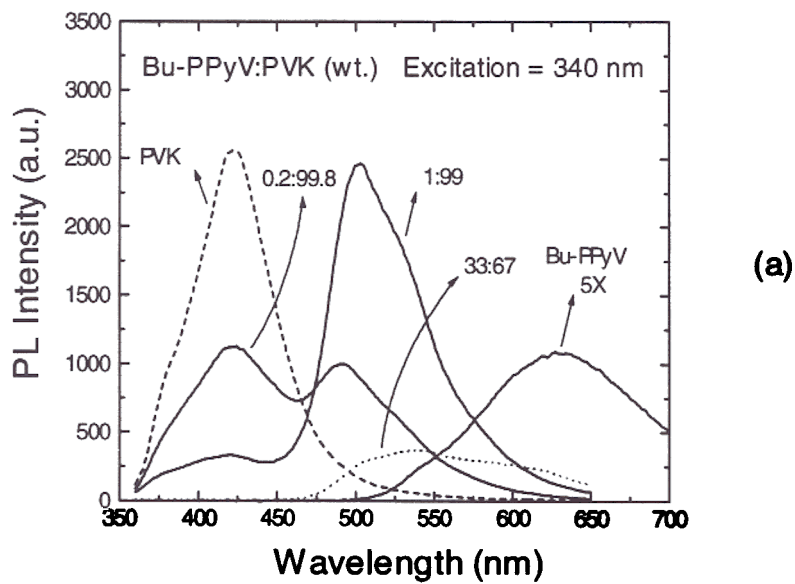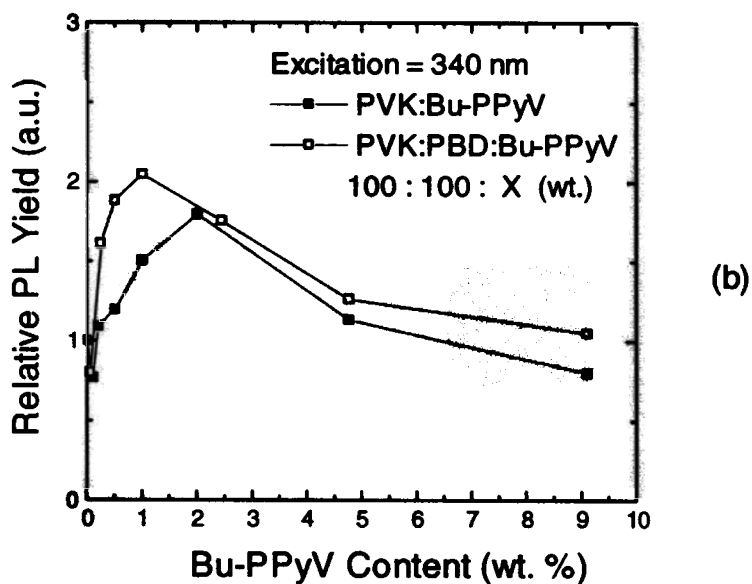
Fig. 4.5: (a) Photoluminescence spectra of Bu-PPyV:PVK blend thin films with different Bu-PPyV content. The excitation wavelength was 340 nm, with most absorption occurring in PVK as Bu-PPyV content is low. (b) Relative integrated photoluminescence efficiencies of PVK:Bu-PPyV and PVK:PBD:Bu-PPyV blend thin films vs. Bu-PPyV content. The strengths were normalized by the absorption at 340 nm in each film.

dopants than that of the host. The enhancement of PL in the present cases indicates that the above three requirements are met to some degree.

4.2.2 Electrochemical Potentials and Energy Levels

In the organic guest-host system or doped carrier-transport polymers, we need to consider not only the energy transfer process, but also the charge transfer or the carrier trapping processes. These characteristics strongly depend on the electrochemical or redox properties of each individual component in the system. We therefore measured the reduction and oxidation potentials of the materials used, in collaboration with Dr. Elena P. Dana in Prof. M. Thompson's lab at University of Southern California.

The reduction and oxidation potentials of materials were determined by electrochemical measurements on a PAR Potentiostat/Galvanostat Model 283. Pt wire was used as the working electrode and the counter electrode. Ag/AgCl served as a reference electrode. Polymers Bu-PPyV and PVK were coated from their solutions in tetrahydrofuran and dichloromethane, respectively, onto the Pt working electrode, electrochemical measurements were performed with the films immersed into the supporting electrolyte solutions (0.05M tetrabutylammonium hexafluorophosphate (TBAHFP) in DMSO for Bu-PPyV and 0.2M $LiClO_4$ in acetonitrile for PVK). Other compounds were used as molecular solutions in DMSO containing 0.05M tetramethylammonium tetrafluoroborate (TMATFB) or acetonitrile containing 0.2M $LiClO_4$. Oxygen was removed from the working solutions by bubbling with argon gas of highest purity. The measured redox potentials vs. Ag/AgCl were later converted to potentials vs. ferrocene-ferrocenium (FOC) redox couple by including the potential difference between FOC and Ag/AgCl in corresponding solutions.

In the electrochemical measurement of polymer films, to maintain overall electrical neutrality, there is diffusion of counter ions from the electrolyte solution into the polymer. While it is not possible to say with certainty what the effect of counter ions is, we

some data on our compounds supporting that this effect is minor. For example, in the case of PVK, we have measured both the polymer film and its monomeric equivalent, N-ethyl-carbazole The monomer is free in the solution and the counter ion effect is far less important. The oxidation potentials measured for both PVK and the monomer are exactly the same, indicating that the counter ion has negligible effect to the electrochemical characterization of PVK. Furthermore, the usual situation where the effect of counter ions is important and gives a system that does not approximate the real system is at extensive reduction or oxidation, where there will be a significant ion incorporation In our electrochemical experiments, only a small fraction of the film is reduced or oxidized, so ion incorporation is at a low level

Cyclic voltammograms of Bu-PPyV, PBD, BND and C6 vs. the Ag/AgCl are shown in Fig. 4.6 The positions of peaks in the negative and positive biases correspond to reduction potentials and oxidation potentials, respectively The values of the redox potentials were obtained by averaging the positions of two peaks occurring in the upward and downward ramp. The cyclic voltammograms of ferrocene-ferrocenium (FOC) vs. Ag/AgCl are also shown in Fig. 4.6 for some solutions The electrochemical potentials of all materials vs. those of the FOC redox couple measured in corresponding solutions used for each material are listed in Table 4.1 Assuming the energy level of FOC is 4.8 eV below the vacuum level, the absolute positions of the HOMO and LUMO levels vs. the vacuum level have been derived from these electrochemical levels [3,4], and are also listed in Table 4.1 For some materials, only reduction or oxidation potentials were successfully obtained, so their HOMO or LUMO levels were estimated by subtracting the apparent optical energy gap (the absorption onset energy, eV) from their LUMO levels or adding the apparent optical energy gap to their HOMO levels [3,4] HOMO levels or LUMO levels estimated this way were marked by an asterisk in Table 4.1. We note that the oxidation potentials and the reduction potentials, of course, correspond to but do not necessarily exactly equal to the HOMO and LUMO levels [3-5], and the evaluation of
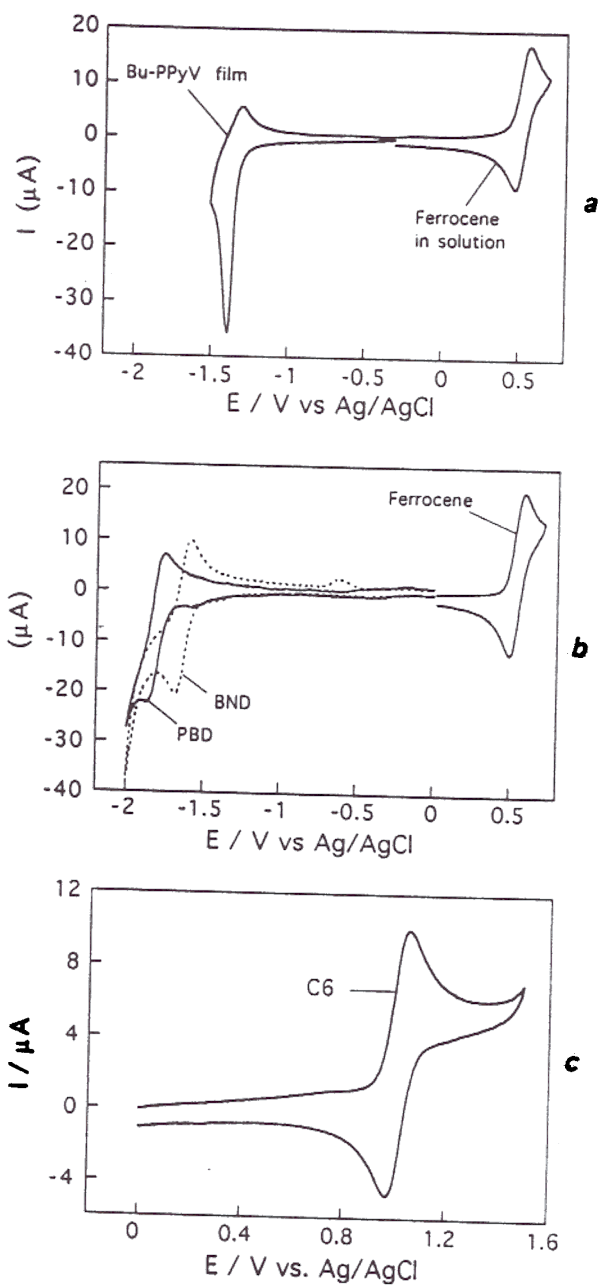
75

Fig. 4.6: Typical cyclic voltammograms from electrochemical spectroscopy. (a) Bu-PPyV as a film at the Pt working electrode and (b) PBD, BND and (c) C6 as 5×10^{-4} M solutions. Supporting electrolytes: (a) 0.05M tetrabutylammonium hexafluorophosphate (TBAHFP) in DMSO, (b) 0.05M tetramethylammonium tetrafluoroborate (TMATFB) in DMSO, (c) 0.2M LiClO$_4$ in acetonitrile. Potential scan rate was 0.1V/s.

Materials	Oxidation Potential	Reduction Potential	Optical Energy Gap	HOMO	LUMO
	(V vs. FOC)		(eV)	(eV vs. vacuum)	
PVK	0.74		3.5	-5.54	-2.04*
Bu-PPyV		-1.87	2.45	-5.38*	-2.93
C6	0.59		2.46	-5.39	-2.93*
C47	0.57		2.88	-5.37	-2.49*
Nile Red	0.5	-1.31		-5.3	-3.49
PBD		-2.34	3.6	-6.06*	-2.46
BND		-2.16	3.3	-5.94*	-2.64
Alq	0.89		2.7	-5.69	-2.99*

Table 4.1: Electrochemical Potentials and Energy Levels of Materials. Electrochemical potentials were measured by cyclic voltammetry. HOMO and LUMO levels were converted from measured electrochemical potentials assuming the absolute energy level of FOC to be -4.8 eV. Values marked by * were estimated from measured HOMO or LUMO levels and optical energy gaps.

HOMO and LUMO levels from electrochemical data in combination with the optical energy gaps is still a matter of debate. However, one should still be able to extract the relative trends of the energy level alignment of HOMOs and LUMOs of different materials from these electrochemical potentials. According to the energy levels listed in Table 4.1, the relative positions of energy levels of PVK, PBD and Bu-PPyV are shown in Fig. 4.7. With such an energy level alignment, Bu-PPyV should be able to trap holes from hole-transport PVK or trap electrons from electron-transport PBD. Also, excited-state charge-transfer exciplexes between Bu-PPyV and PVK or PBD should not be expected as is consistent with the photoluminescence experiments. Instead, such an energy level alignment is not in conflict with any energy transfer process since the Bu-PPyV has a lower energy gap and its energy levels lie between those of PVK and PBD.

4.3 Blend Devices Using Bu-PPyV as Emission Centers

In this section, we discuss the electroluminescence of three different structures: ITO/PVK:Bu-PPyV (1050 Å)/Mg:Ag (1200Å)/Ag (800Å), ITO/PVK:PBD:Bu-PPyV (1050 Å)/Mg:Ag (1200 Å)/Ag (800 Å) and ITO/ PVK:BND:Bu-PPyV (1050 Å)/Mg:Ag (1200 Å)/Ag (800 Å), with various blend compositions. All the ITO/glass substrates used in this section were treated with the oxygen plasma in the Plasmod reactor, which has been discussed in Section 3.3.

4.3.1 PVK:Bu-PPyV Blends

First, the PVK:Bu-PPyV system was studied. In general, in going from pure PVK to pure Bu-PPyV, the electroluminescence of PVK:Bu-PPyV blends goes through the transition from deep blue PVK emission to green emission of isolated Bu-PPyV chromophores and then to red emission of Bu-PPyV excimers, spanning the whole visible spectrum from this single series of blends as shown in the spectra of Fig. 4.8. Fig. 4.9
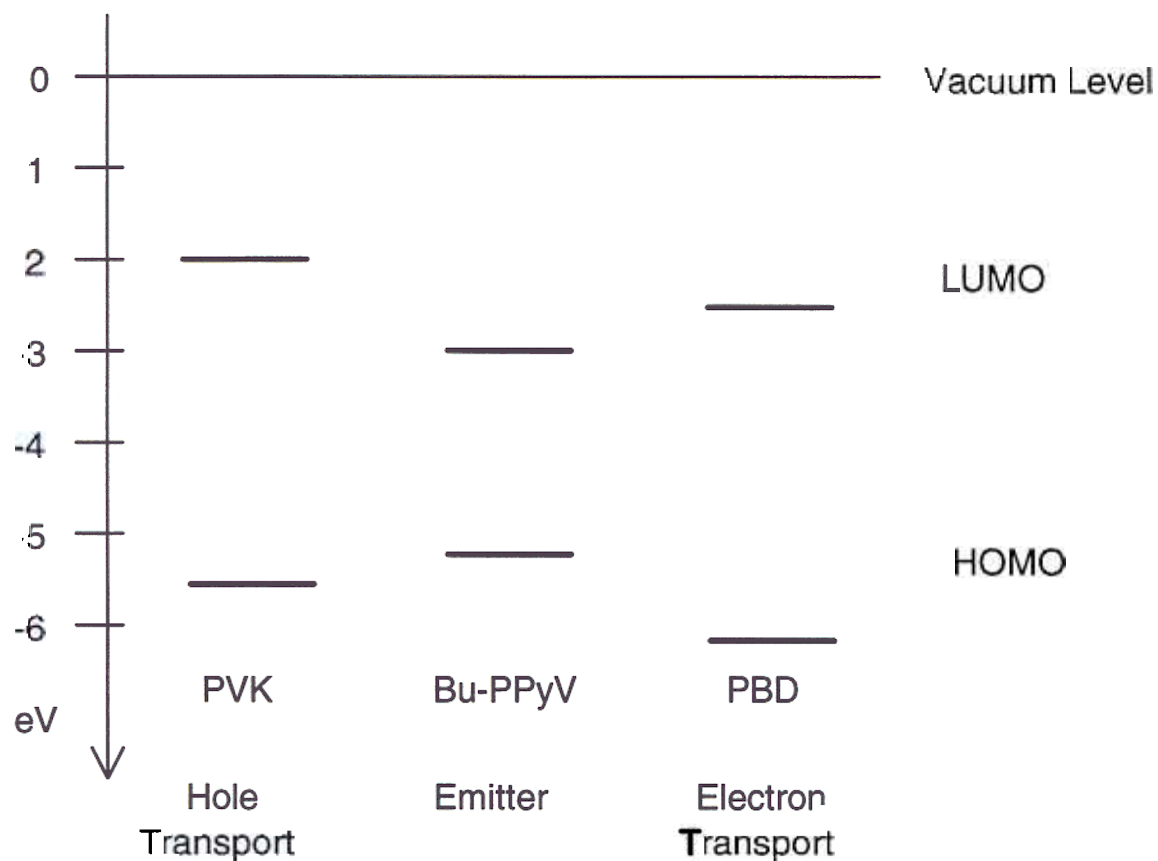
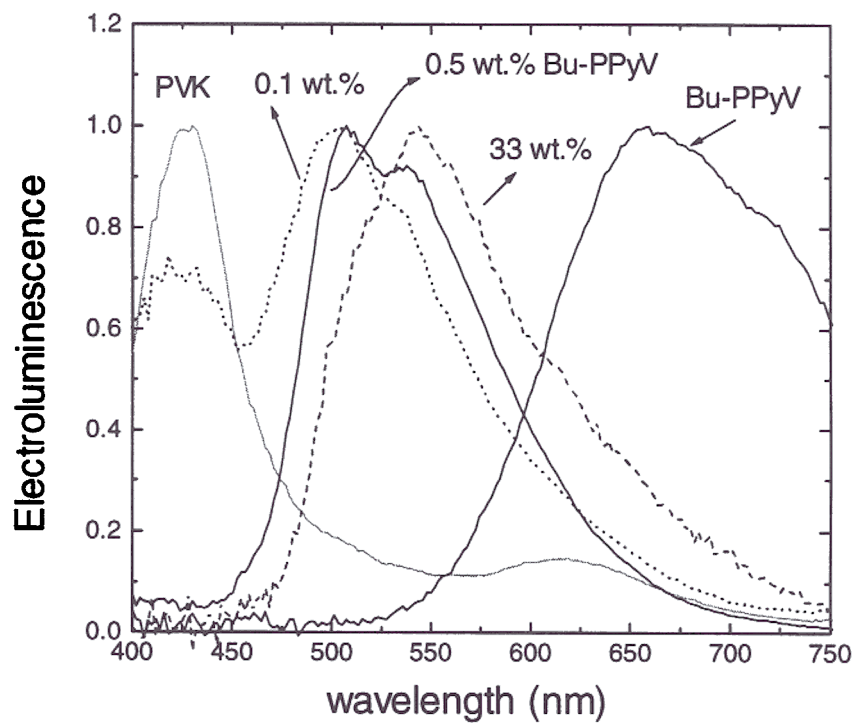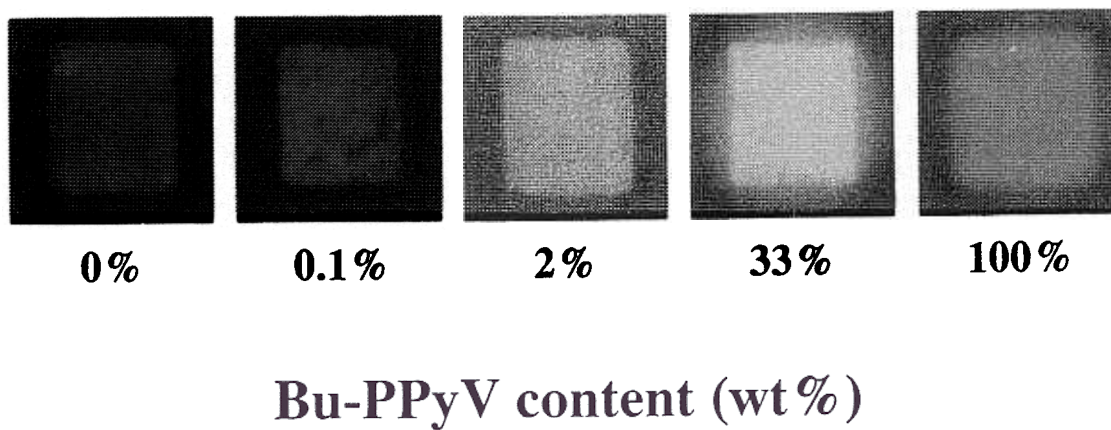Fig   Relative energy level alignment for PVK, Bu-PPyV and PBD according   the values listed in **Table 4.1**

Fig. 4.8: Normalized EL spectra of PVK:Bu-PPyV devices of different Bu-PPyV contents.

0% 0.1% 2% 33% 100%

Bu-PPyV content (wt%)

Fig. 4.9: Photographs of working EL devices made from PVK:Bu-PPyV blend thin films of different ratios. Pure PVK devices emit purple-deep blue light. With extremely low Bu-PPyV content, the blend film emit blue-green light, a combination of PVK and isolated Bu-PPyV chromophore emissions. Green emission is from isolated Bu-PPyV chromophores. With higher Bu-PPyV content, the emission shifts to yellow and eventually to weak red emission of Bu-PPyV excimers.

shows the color photographs of these devices. The dependence of external EL quantum efficiency on the content of Bu-PPyV in PVK:Bu-PPyV is shown in Fig. 4.10, along with the relative PL efficiency (340 nm excitation). The EL efficiency first increases rapidly with Bu-PPyV content from 0.03% (photon/electron) for pure PVK to 0.3% at 0.5 wt.% Bu-PPyV content. The following drop of EL efficiency with further addition of Bu-PPyV above 1 wt.% is due to the reduced PL efficiency for these emission centers as shown in Fig. 4.2(b) or Fig. 4.5(b). The large initial increase in EL efficiency (10 times), however, cannot be accounted for simply by the modest increase in the PL efficiency of the host matrix PVK (~2 times in Fig. 4.5(b)) caused by doping with Bu-PPyV, in which we assume excitons are first formed on the host and then transferred to the more radiatively efficient Bu-PPyV centers. Instead, this indicates that the observed enhancement of EL efficiency is mostly due to a significant enhancement of carrier recombination on Bu-PPyV centers, suggesting the direct formation of excitons on Bu-PPyV centers by sequential trapping of oppositely charged carriers. The trapped or more localized electrons or holes on these centers can then more easily capture the opposite carriers and form excitons, followed by efficient radiative recombination. This hypothesis is further supported by the difference between PL spectra (Fig. 4.5(a)) and EL spectra (Fig. 4.8) of PVK:Bu-PPyV blends at low Bu-PPyV content. For example, in PL using 340 nm excitation wavelength to create excitons in PVK, at 0.2 wt.% of Bu-PPyV most of the luminescence is still from PVK, whereas in EL, at 0.1 wt.% of Bu-PPyV, Bu-PPyV luminescence already dominates since more efficient carrier recombination can take place directly on the Bu-PPyV centers in the case of EL.

4.3.2 PVK:PBD:Bu-PPyV Blends

PVK is well known as a hole-transport polymer [6-9], with hole transport through the side-chain carbazole group and with only extremely limited electron-transport ability, if any. Therefore, though there is a large enhancement of EL in PVK:Bu-PPyV
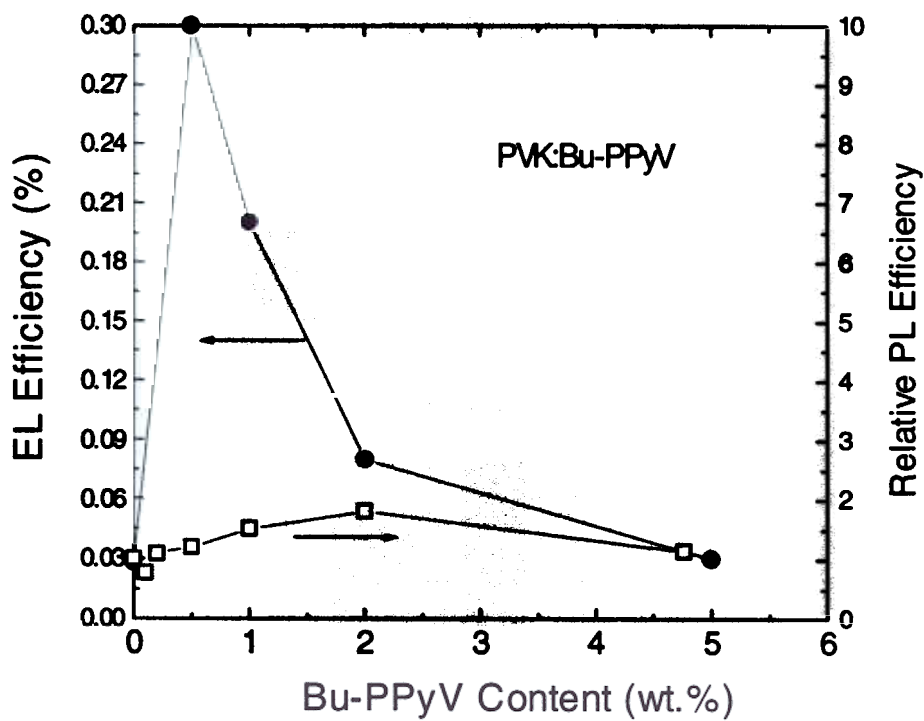
Fig. 4.10: External EL efficiency of ITO/PVK:Bu-PPyV (1050 Å)/Mg:Ag (1200 Å)/Ag 800 Å) devices vs. Bu-PPyV content. The relative PL efficiency (340 nm excitation) of PVK:Bu-PPyV blend thin films plotted in **Fig. 4.5** is also shown for comparison.

compared with pure PVK, device performance is thought to be still limited by the electron injection/transport ability of PVK. First of all, the imbalance between holes and electrons leads to inefficient utilization of carriers. Also, due to the unbalanced hole and electron transport properties in the single-layer PVK:Bu-PPyV devices, it is possible that recombination takes place very close to the organic/metal cathode interface, which itself could be a quenching site [10,11]. To improve the electron injection/transport ability of the films, the electron-transport oxadiazole PBD [12] was added. The external EL efficiency vs. the Bu-PPyV content in PVK:PBD:Bu-PPyV system is shown in Fig. 4.11. The external EL efficiency vs. the PBD content is shown in Fig. 4.12. As in the PVK:Bu-PPyV system shown in Fig. 4.10, the EL efficiency peaks at a Bu-PPyV content below 1 wt.%. The addition of PBD can further enhance the external EL efficiency several fold compared to that without PBD. The highest external EL efficiency of 0.8% is achieved with a PVK to PBD ratio of about 100:40-50 (by weight). Again, the large enhancement of EL with Bu-PPyV doping (~10 times) over PVK:PBD cannot be accounted for by the modest PL enhancement of the host, suggesting the same carrier trapping mechanism for EL enhancement as in the PVK:Bu-PPyV case. The difference between the EL and PL spectra again supports this hypothesis. In EL, no emission other than that of Bu-PPyV can be detected for Bu-PPyV contents as low as 0.05 wt.% in the PVK:PBD:Bu-PPyV blends, while at that Bu-PPyV content, the emission from PVK:PBD still dominates the PL. Therefore, in PVK:PBD:Bu-PPyV system, carrier trapping is an even more favored mechanism than energy transfer.

The addition of PBD also has a tremendous effect on the I-V characteristics of the devices, as shown in Fig. 4.13. For all devices with identical thickness (~1050 Å), the rise of forward current with voltage first gets steeper with PBD addition, leading to a reduction in the operating voltage of the devices. However, increasing the PVK:PBD weight ratio beyond 100:50 does not further enhance the current. Instead, the I-V curve is bent down again and the EL efficiency is reduced. Fig. 4.14 shows the effect of the
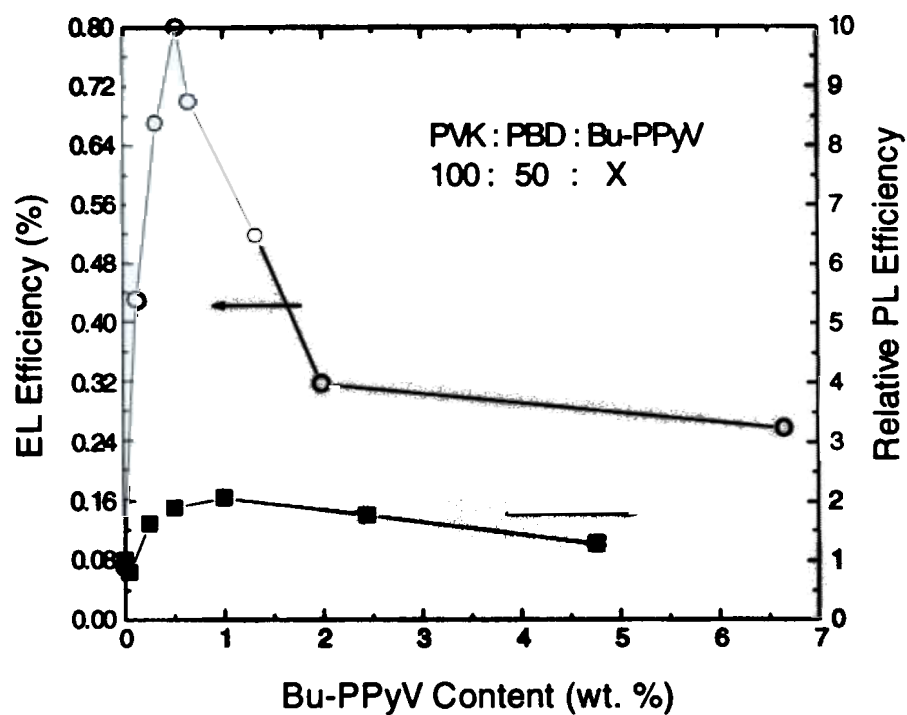
Fig. 4.11: External EL efficiency of ITO/PVK:Bu-PPyV (1050 Å)/Mg:Ag (1200 Å)/Ag (800 Å) devices vs. Bu-PPyV content. The relative PL efficiency (340 nm excitation) of PVK:Bu-PPyV blend thin films plotted in **Fig. 4.5** is also shown for comparison.
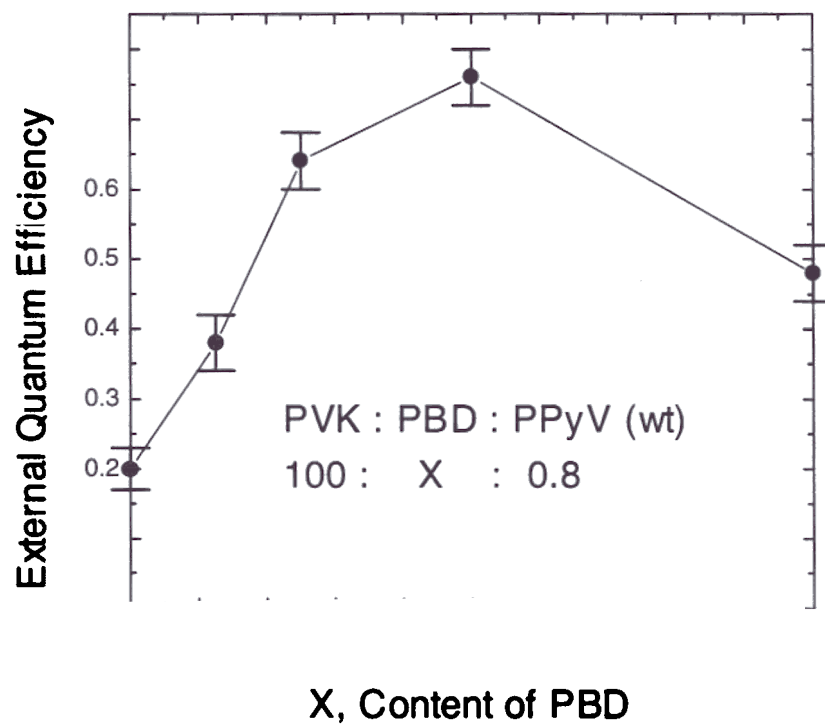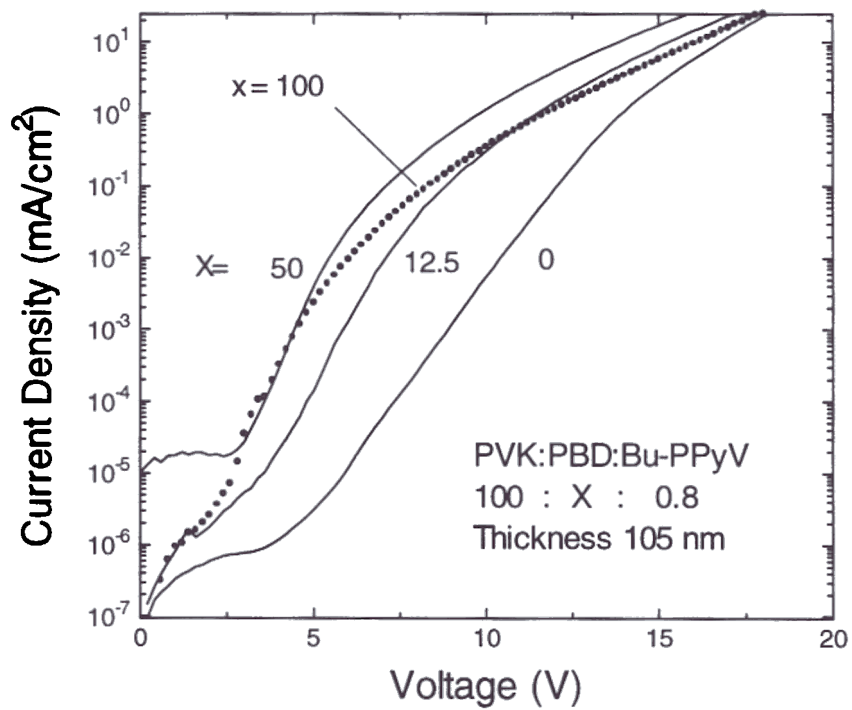
Fig. 4.12: External EL efficiency of ITO/PVK:PBD:Bu-PPyV (1050 Å) /Mg:Ag (1200 Å)/Ag (800 Å) devices vs. content of PBD.

Fig. 4.13: Forward I-V characteristics of ITO/PVK:PBD:Bu-PPyV (1050 Å)/Mg:Ag (1200 Å)/Ag (800 Å) devices of different PBD contents.
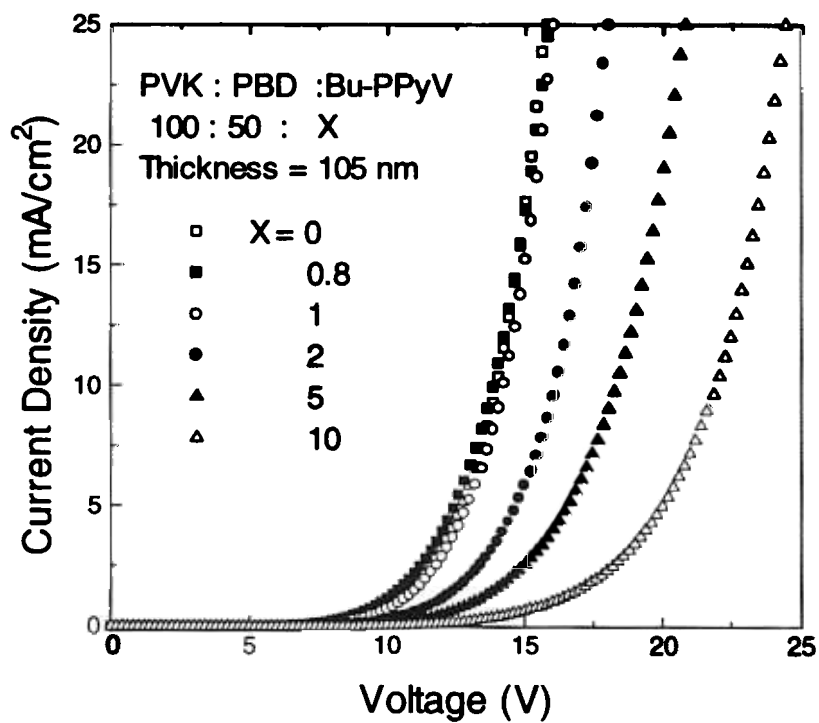
Fig. 4.14: Forward I-V characteristics of ITO/PVK:PBD:Bu-PPyV (1050 Å)/Mg:Ag (1200 Å)/Ag (800 Å) devices of different Bu-PPyV contents. PVK:PBD ratio is 100:50 by wt.

addition of Bu-PPyV on the electrical characteristics of PVK:PBD:Bu-PPyV devices. With very low doping by Bu-PPyV (< 1 wt. %), there is no significant change of the I-V characteristics compared to devices without Bu-PPyV doping. Therefore, there is no significant tradeoff between the optimal doping for EL and keeping the operating voltage low. When the Bu-PPyV doping level is raised above 1 wt. %, the shift of I-V characteristics to higher voltages becomes significant, indicating that the carrier transport properties of the host are perturbed by the doped Bu-PPyV. The results are consistent with the lowering of carrier mobility in a carrier transport medium doped with carrier trapping centers [13,14].

4.4 Devices Using Organic Dyes as Emission Centers

We have also explored the use of molecular dyes instead of Bu-PPyV as the emitting dopants. Since the emission from the blend is basically that of the emitting dopant, replacing Bu-PPyV with other centers which emit efficiently in different parts of the visible spectral range and have appropriate redox properties so that all materials have an energy level alignment similar to that in Fig. 4.7 would permit color tuning for EL devices. Since both PVK and oxadiazoles fluoresce at energies higher than blue light, color tuning up to blue is possible.

Fig. 4.15 shows the EL spectra of blue, green and orange devices made from molecularly doped PVK, with either PBD or Alq as electron-transport molecules. emitting dopants used are commercial organic laser dyes or pigments: coumarin 47 (C47), coumarin 6 (C6) and nile red for blue, green and orange EL, respectively. composition of each blend was optimized following the similar strategy described in previous sections. The detailed blend compositions for the blue, green and orange devices are listed in Table 4.2. The luminous efficiencies (lumen/light watt) for each color calculated from their EL spectra in Fig. 4.15 are also listed in Table 4.2.
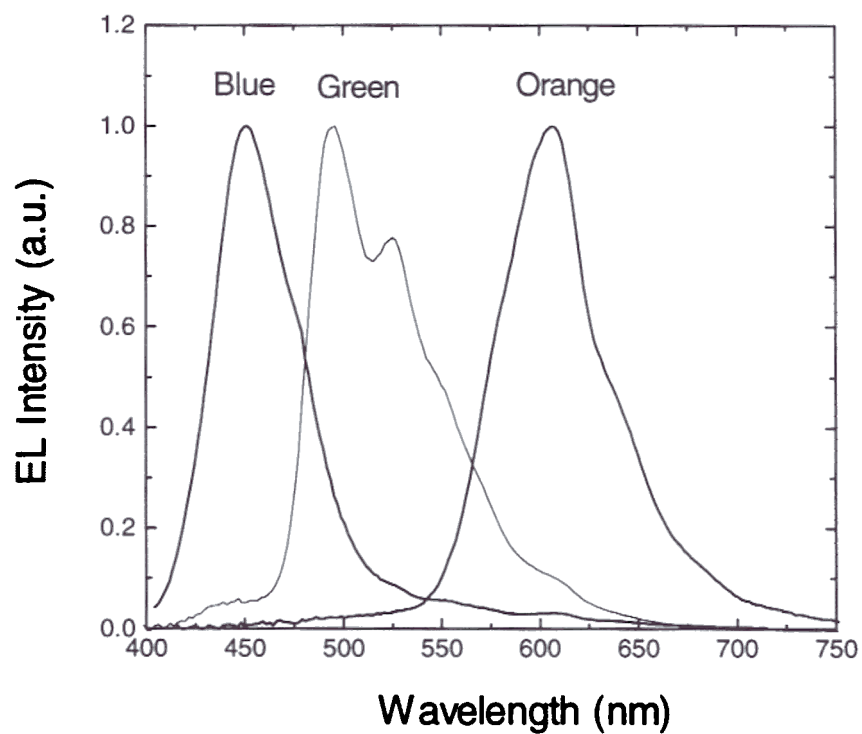
Fig. 4.15: EL spectra of blue, green and orange devices, the compositions of which are ITO/PVK:PBD:C47 (100:40:1 by wt.)/Mg:Ag/Ag, ITO/PVK:PBD:C6 (100:40:0.3 by wt.)/Mg:Ag/Ag and ITO/PVK:Alq:nile red (100:40:0.2 by wt.)/Mg:Ag/Ag, respectively.

	Blend Composition (by wt.)	Luminous Efficiency (lm/light watt)
Blue	PVK:PBD:C47 (100:40:1)	115 lm/W
Green	PVK:PBD:C6 (100:40:0.3)	410 lm/W
Orange	PVK:Alq:Nile red (100:40:0.2)	420 lm/W

Table 4.2: Blend compositions and luminous efficiencies for blue, green and orange devices.

Fig. 4.16(a) and Fig. 4.16(b) show I-V-L characteristics and I-L characteristics of the blue, green and orange devices composed of the oxygen plasma-treated ITO anode, ~1000-Å-thick blend thin films of the above compositions, and the Mg:Ag(1200 Å)/Ag (800 Å) cathode. All these devices have quite similar I-V characteristics. Currents start rising rapidly between 2-4V, with light emission becoming detectable between 3-5V, correspondingly. Other groups have reported similar PVK-based single-layer devices, but such low turn-on voltages have previously never been reported. With similar film thicknesses, the turn-on voltages of ~3-5V in our devices are much less than the turn-on voltages of ~10-30V in previous work [15-19]. The main obvious difference in our work is the improvement of the ITO anode contact to the blend OLEDs via oxygen plasma treatment, which has been found to modify the surface composition and the surface work function [20]. The hole-injection efficiency and the performance of the single-layer doped-polymer OLEDs are thus substantially enhanced. The effect of the ITO treatment on devices will be further discussed in chapter 5.
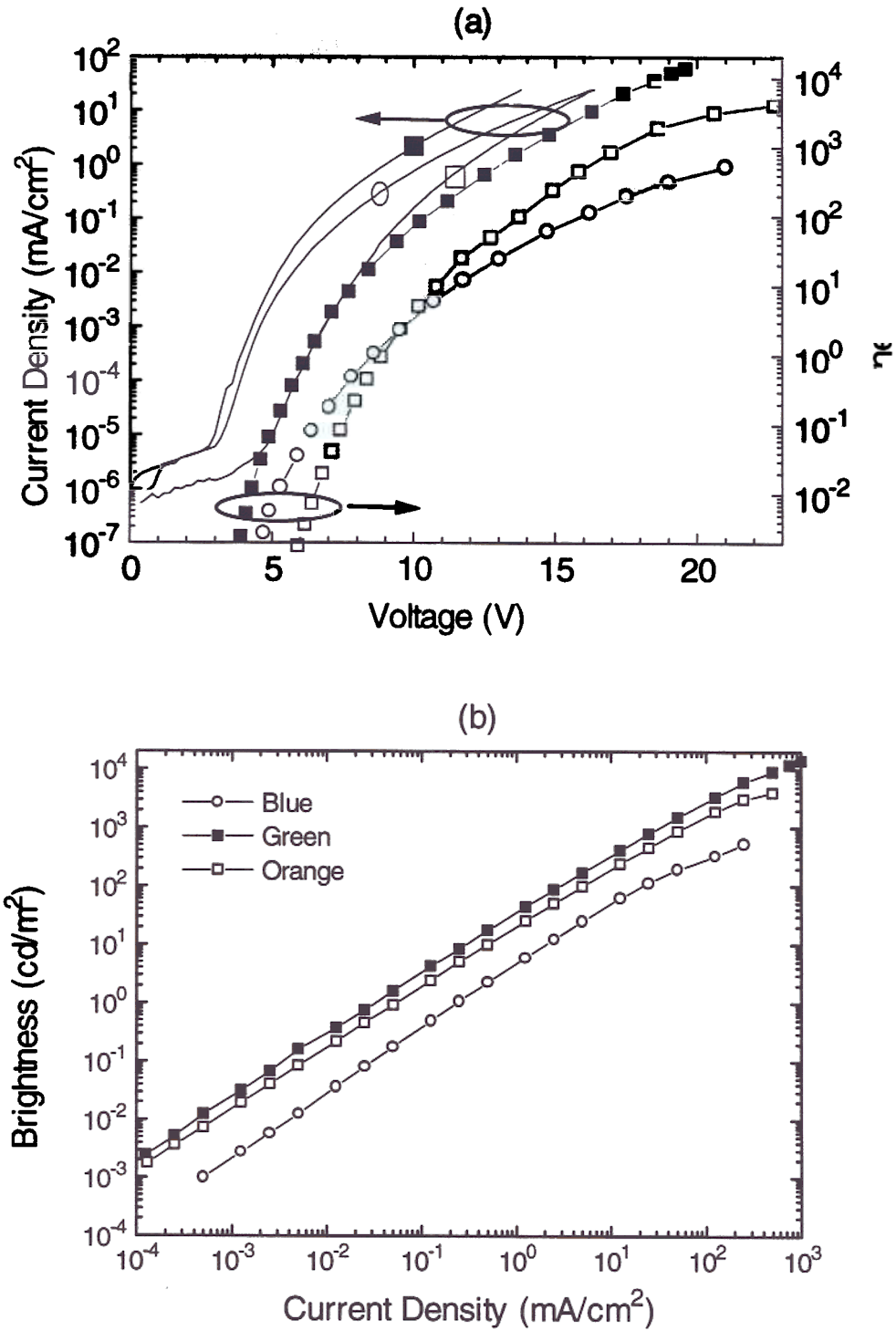
Fig. 4.16: Forward Current-Voltage-Brightness characteristics of the blue (open circle), green (solid square) and orange (open square) devices, whose spectra are shown in Fig. 4.15.

	Blue	Green	Orange
$\eta_{ext.}$ (photon/e, %)	0.5	1.1	0.7
cd/A	0.5	3.6	2
Voltage at 10 cd/m^2, V	11	8	11
Voltage at 100 cd/m^2, V	15	10	14
Luminous efficiency (lm/W) at 10 cd/m^2	0.14	1.4	0.6
Luminous efficiency (lm/W) at 100 cd/m^2	0.1	1.1	0.5

Table 4.3: A summary of device performance for the blue, green and orange devices.

Table 4.3 gives a summary of device performance for the blue, green and orange devices. In these devices, practical brightnesses of 10-100 cd/m^2 can be achieved at ~10V. High brightnesses of ~4,000 cd/m^2, ~10,000 cd/m^2 and ~500 cd/m^2 are obtained at a higher operating voltage (~20V) for orange, green and blue devices, respectively. The external EL efficiencies for the blue, green and orange devices are 0.5%, 1.1% and 0.7%, respectively. The luminous efficiencies of devices vs. the brightness levels are shown in Fig. 17. Since the luminous efficiency is proportional to (light output)/(I×V), it drops gradually as the brightness level and therefore the drive voltage are raised. The luminous efficiencies at 100 cd/m^2 for the blue, green and orange devices are 0.1 lm/W, 1.1 lm/W and 0.5 lm/W, respectively.

The electrochemical potentials of the dyes used were measured and are also listed in Table 4.1 with those of other materials described earlier. From the energy levels listed in Table 4.1, the energy level alignment for the above blue, green and orange devices is similar to that in Fig. 4.7, i.e. the HOMO/LUMO levels of the emitting dopants lying within the bounds set by the HOMO level of PVK and the LUMO level of electron-
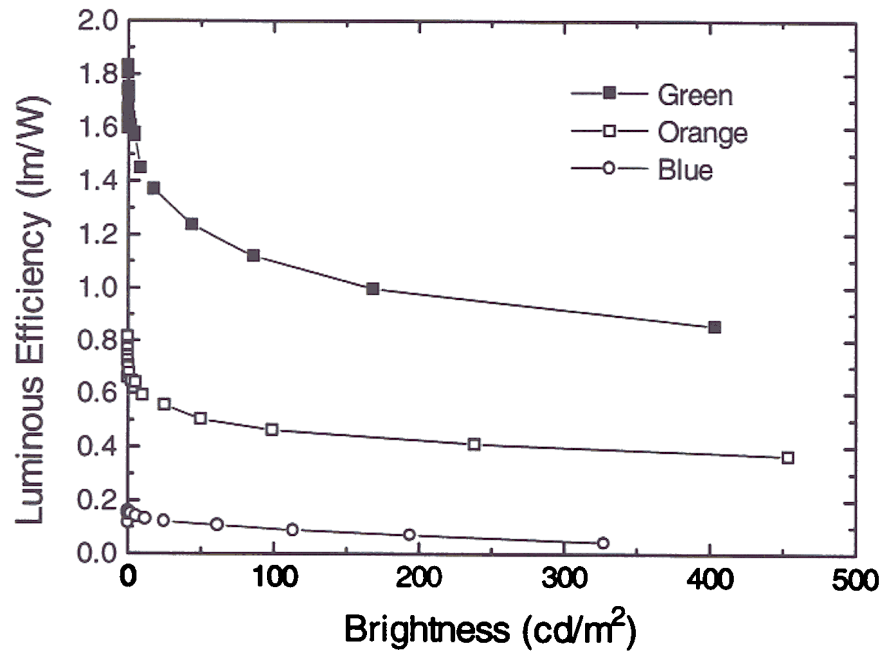
Fig. 4.17: Luminous efficiencies of the blue, green and orange devices vs. brightness level.

transport molecules. C6 has also been used as the emitting dopant in the PVK:Alq blends to make green OLEDs. The PVK:Alq:C6 devices are not as efficient as PVK:PBD:C6 devices. In addition, the dependence of EL efficiency on the C6 concentration in these two devices are different, as shown in Fig. 4.18. The EL efficiency of the PBD devices rises rapidly in the C6 concentration range of 0-0.3 wt.% and drops fast beyond this range. The EL efficiency of the Alq devices, however, increases slowly with the C6 concentration in a much larger range of 0-1.5 wt.%. From the LUMO levels (Table 4.1) of PBD (-2.46 eV), Alq (-2.99 eV) and C6 (-2.93 eV), we found that the LUMO levels of C6 and Alq are very close. Therefore, C6 dopants might not be as efficient in trapping electrons from Alq as from PBD. The enhancement of EL by direct formation of excitons on the C6 dopants in Alq devices is therefore not as strong as in the PBD devices, particularly when the concentration of C6 is low.

4.5 Discussion

Before any detailed modeling of the single-layer doped polymer OLEDs can be carried out, it is necessary to consider the behavior of the charge carriers throughout the entire device, including the anode/organic contact, the organic bulk and the cathode/organic contact. Depending on the contacts, the bulk properties of the organic layers and the bias applied, the behavior can in principle change among monopolar space-charge limited (SCL) current, bipolar space-charge limited current, and injection-limited current [21,22]. In the case of optimized doped polymer OLEDs, the reasonable EL efficiency suggests of comparable injection abilities for both holes and electrons. It is therefore a double-carrier injection problem and cannot be simplified to a (relatively) easier single-carrier injection problem. In general, the analysis is complicated by how to describe each injection process (ohmic [21,22], Schottky [23] or tunneling [24] etc.), the recombination process, or the energetics of the defect states at the interfaces and in the
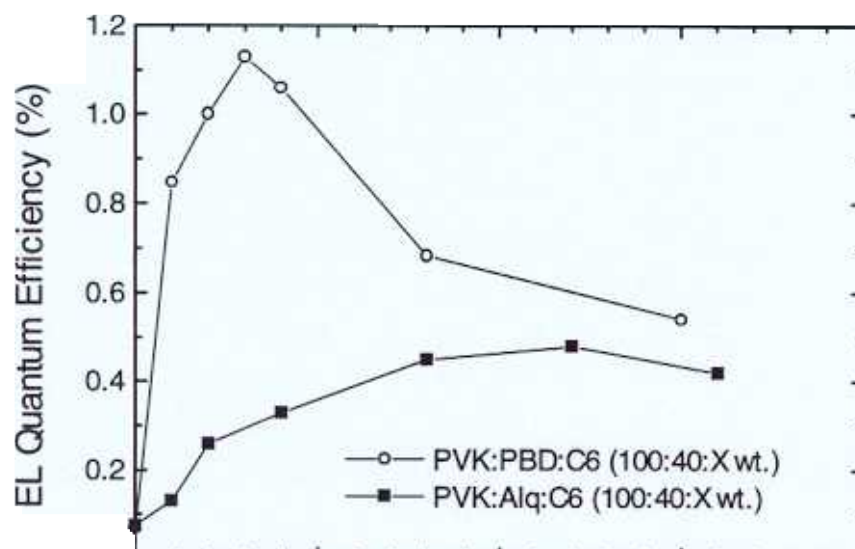
95

Fig. 4.18: External EL quantum efficiency vs. C6 concentration in ITO/PVK:Alq:C6 (100:40:X wt., ~1000 Å)/Mg:Ag (1200 Å)/Ag (800 Å) and ITO/PVK:PBD:C6 (100:40:X wt., 1050 Å)/Mg:Ag (1200 Å)/Ag (800 Å).

bulk which affect the carrier trapping and the recombination. There is no universal analytical model that has been developed to handle such a general double-carrier injection devices.

To get deeper insight into the operation of the doped polymer OLEDs, in this section we first treat simpler cases, such as the single-carrier devices and the ideal two-carrier devices. In Section 4.5.1, the better developed analytical models for the current flow in single-carrier devices are reviewed and are compared with the experimental results. In Section 4.5.2, we review the analytical model for an ideal two-carrier SCL current with trap-free transport and two ohmic contacts, which is the only existing analytical model for double-carrier injection into low mobility materials. Based on the concepts and conclusions established in Section 4.5.1 and Section 4.5.2, we then give qualitative discussions to some details of the device characteristics of the single-layer doped polymer OLEDs in Section 4.5.3.

4.5.1 Analytical Models for Single-Carrier Devices

Before the more complicated PVK:oxadiazole:fluorescent dopant systems are discussed, it would be useful to examine the single-carrier PVK devices first. The current flow in a single-carrier device could be controlled either by the bulk properties of the organic layer or the carrier injection from the contact. In the following, one bulk-limited process, the trapped-charge-limited (TCL) current, and two injection-limited processes, the Fowler-Nordheim tunneling and the thermionic emission, are examined.

Fig. 4.19(a) shows the I-V characteristics for the ITO/PVK/Mg:Ag/Ag devices with different PVK thicknesses. These devices are not perfect single-carrier devices because the Mg:Ag cathode contact still can inject electrons into the PVK layer. However, considering the relatively low EL efficiencies (~0.01%) of these devices and the much lower mobility of electrons than that of holes, we assume that the I-V characteristics of these devices are mainly governed by holes and that they can be approximated as single-
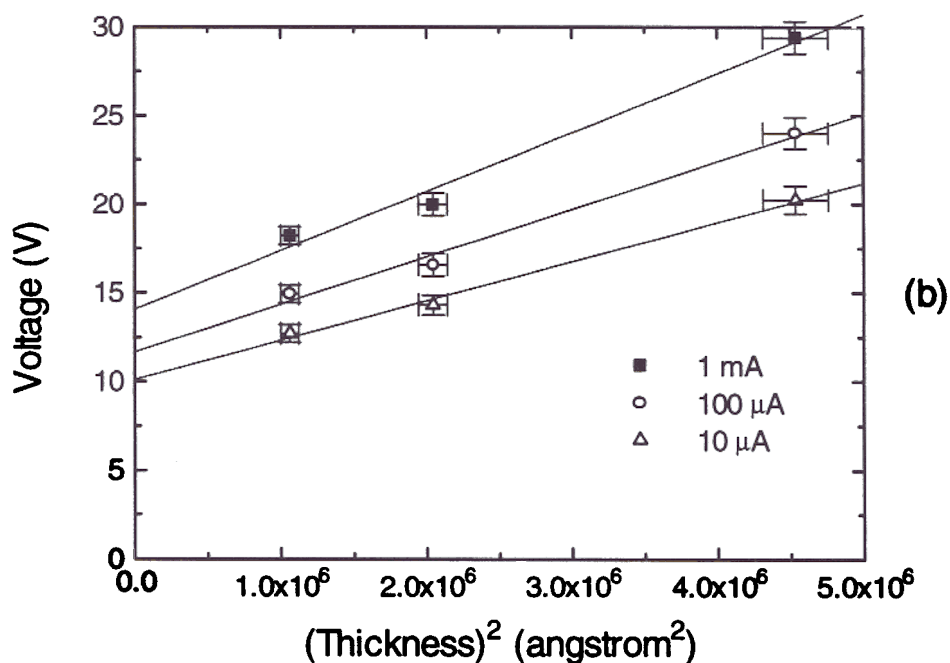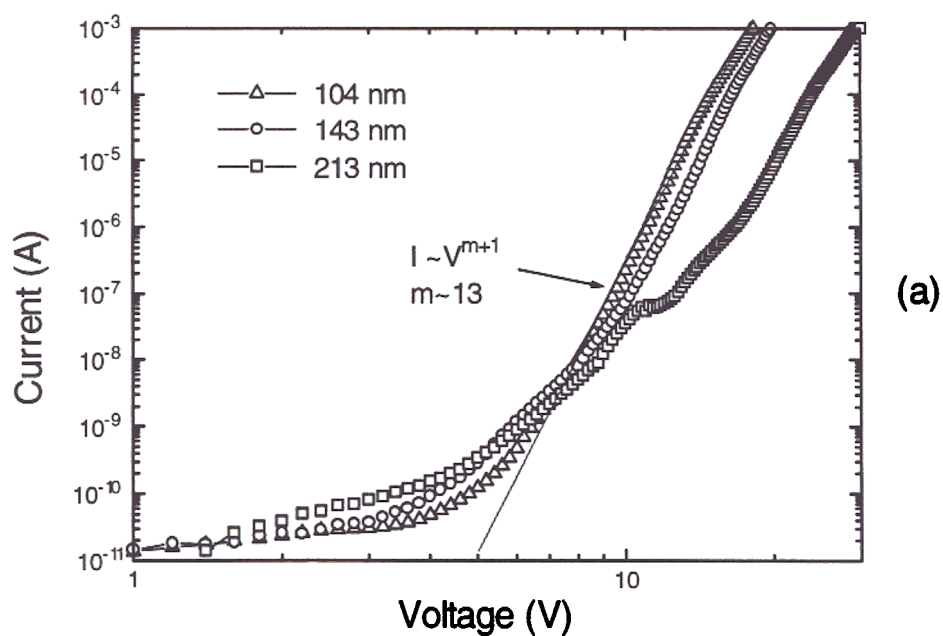
97

Fig. 4.19: (a) Forward I-V characteristics of ITO/PVK/Mg:Ag (1200 Å)/Ag (800 Å) devices with different PVK thicknesses. (b) V-L^2 plots of Fig. 4.19(a) for different current levels. The device area is 2mm×2mm.

carrier devices. In all these I-V curves, the current strongly increases for voltages above a critical voltage. The occurrence of an abrupt increase of the current at a certain critical voltage is a characteristic usually seen for a low-mobility material with carrier traps [21,22]. For trap levels located at a single energy, this trapped-charge-limited (TCL) current regime is an extremely sharp transition, at which the current directly switches to the trap-free SCL current. The more gradual increase points to a distribution of trap-level energies and is usually well described by an exponential distribution of traps:

$$p_t(E) = (\frac{N_t}{kT_t}) \exp(\frac{E_v - E}{kT_t})$$

(4.1)

with p_t (E) the hole trap density of states at energy E, E_v the energy of the valence (HOMO) band edge, N_t the total density of traps and kT_t an energy characterizing the trap distribution. The trap distribution of Eq. (4.1) implies for the voltage dependence of the current density J in the TCL regime [21,22]:

$$J = N_v q \mu_p (\frac{\varepsilon}{qN_t})^m \frac{V^{m+1}}{L^{2m+1}} C(m)$$

(4.2)

with $m = T_t/T$, ε the permitivity of the organic layer, N_v the effective density of states in the valence (HOMO) band, μ_p the mobility of holes, L the thickness of the sample, and $C(m) = m^m(2m+1)^{m+1}(m+1)^{-(2m+1)}$.

It should be noted from Eq. (4.2) that the trap distribution parameter T_t not only determines the slope of the logI-logV plot, but also the thickness dependence in the TCL regime. According to Eq. (4.2), V is approximately proportional to L^2 at a constant current if m >>1. This is checked in Fig. 4.19(b) by replotting the data of Fig. 4.19(a). From Fig. 4.19(b), it is seen that the linear fits of V-L^2 data intersect the V-axis at voltages comparable to the whole drive voltage. This is not consistent with the TCL description, which predicts the intersection voltage of the linear V-L^2 plots to be close to

zero. It should be noted that the validity of Eq. (4.2) is based on the assumption that the contact is rather "ohmic", that is, the voltage across the contact is small compared to the voltage across the bulk and the boundary condition for the electric field distribution at the injection contact is small compared to the maximum field in the bulk [21,22]. Under such conditions the I-V characteristics are then governed by the bulk properties, such as the carrier mobility and the trap density. The TCL I-V characteristics have been well documented for OLED devices and materials [25-29]. A good example from the literature [26] is given in Fig. 4.20(a), where the I-V characteristics for glass/Ca/PPV/Ca devices with different PPV thicknesses are shown. The top Ca/PPV contact is ohmic for electron injection and the bottom Ca/PPV contact is blocking for hole injection. The observed I-V characteristics are therefore attributed to the bulk transport properties of electrons in the PPV. To check if the Ca/PPV contact for electron injection is really ohmic, we replot the data of Fig. 4.20(a) in the V-L^2 format in Fig. 4.20(b). The Ca/PPV ohmic contact is confirmed by the linear V-L^2 relationship and nearly zero intersection voltage at the V axis. From these examinations, we therefore conclude that the ITO/PVK contact is not ohmic and that the injection process also has significant contribution to the I-V characteristics of PVK devices.

We have now established that the contacts are a major source of the voltage drop in the PVK devices. We now examine two models of contacts (Fowler-Nordheim tunneling and thermionic emission) to see if they can account for the observed voltage drop in our devices.

It has been proposed [30] that the I-V characteristics of single-layer polymer OLEDs are controlled by Fowler-Nordheim tunnelling of both electrons and holes through contact barriers between the electrode and the organic layer, with a rather uniform electric field across the organic film (i.e. minor space-charge effect). Assuming a triangular barrier at the electrode-organic interface under an applied electric field F, the Fowler-Nordheim tunneling theory predicts [24]
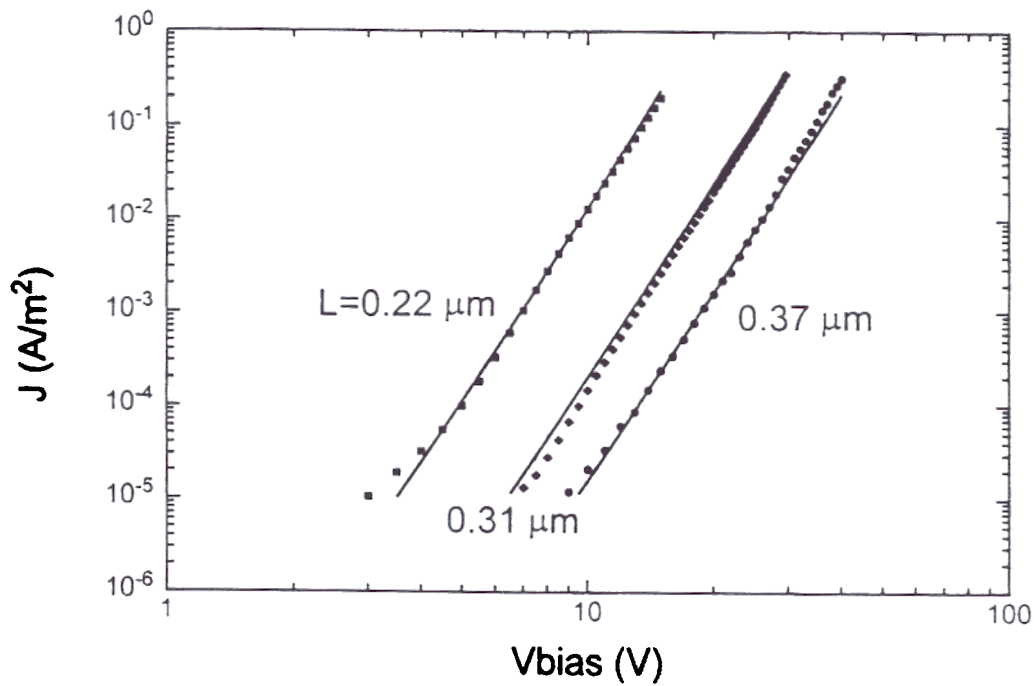
(a)
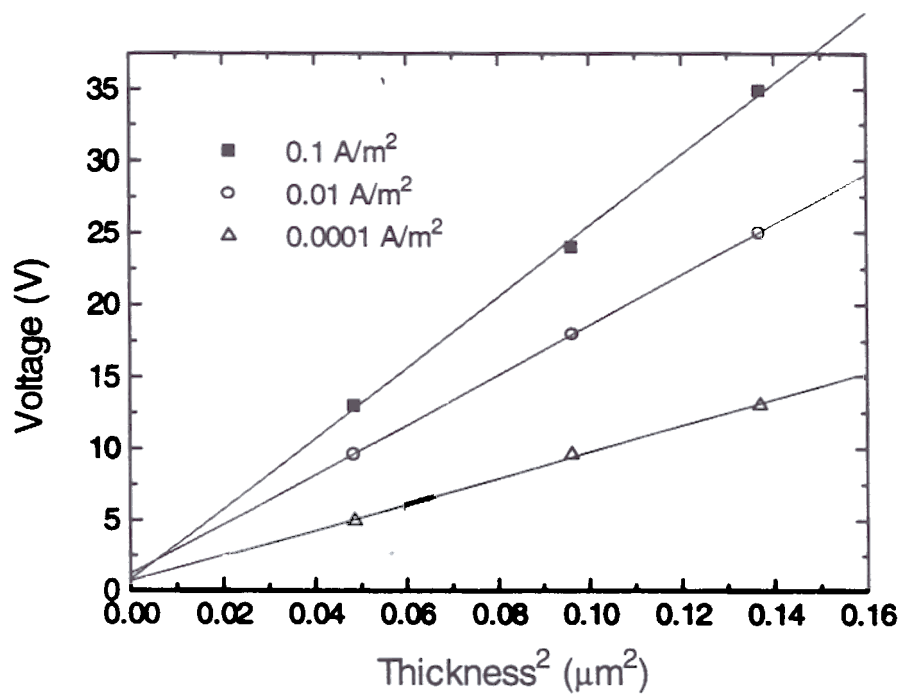
(b)

Fig. 4.20: (a) Thickness dependence of the I-V characteristics for the electron-only glass/Ca/PPV/Ca devices. (b) V-L^2 plots of Fig. 4.20(a) for different current levels. (from Ref. [26])

$$J = (\frac{q^3}{\_o\sim\_{L}})\frac{F^2}{\phi}\exp[(\frac{8\pi\sqrt{2m^*}}{3qh})\frac{-\phi^{3/2}}{F}]$$

with h the Planck's constant, ϕ the barrier height and m^* the effective mass of the charge carrier. Fig. 4.21 shows a plot of $\log(I/F^2)$ vs. $1/F$ for an ITO/PVK/Mg:Ag/Ag device. In general, the I-V only follows the Fowler-Nordheim relation over a limited (high) voltage range. Fitting the I-V in the high field regime yields an ITO/PVK barrier height of ~0.22 eV, assuming the effective mass equals to the free electron mass. With this barrier height, the currents predicted from Eq. (4.3) exceed the measured currents by several orders of magnitude at high fields, as shown in Fig. 4.22 The tunneling alone therefore does not seem to give a proper description of the I-V characteristics observed in the present devices.

Another well-known injection process is the thermionic emission of carriers across the electrode-organic barrier ϕ . For current injection into low-mobility materials, the diffusion effect has to be considered [21,31]. The diffusion-limited thermionic emission theory gives [31]

$$J = qN_v\mu_pF\exp[\frac{-q}{kT}(\phi - \sqrt{\frac{qF}{4\pi\varepsilon}})]$$

where the lowering of the barrier height by the image force effect with the applied field F at the contact is also included. In Fig. 4.22, the current predicted by Eq. (4.4) is plotted against V for a device with $L = 100$ nm, $F = V/L$, $\mu_p = 2\times10^{-6}$ cm^2/V·s, $\phi = 0.4$ eV, ε $3\varepsilon_0$, and $N_v = 2.5\times10^{19}$ cm^{-3}. In comparison with the measured I-V characteristics, the currents predicted by Eq. (4.4) shows a much more gradual variation with the voltage and does not have any resemblance to the measured characteristics.

From the above examination, we are led to the conclusion that in our devices both the bulk transport and contact effects contribute significantly to the device voltage because there is no single bulk-limited or injection-limited process which can give reasonable description of the device I-V behavior. It, however, suggests that it is possible to further
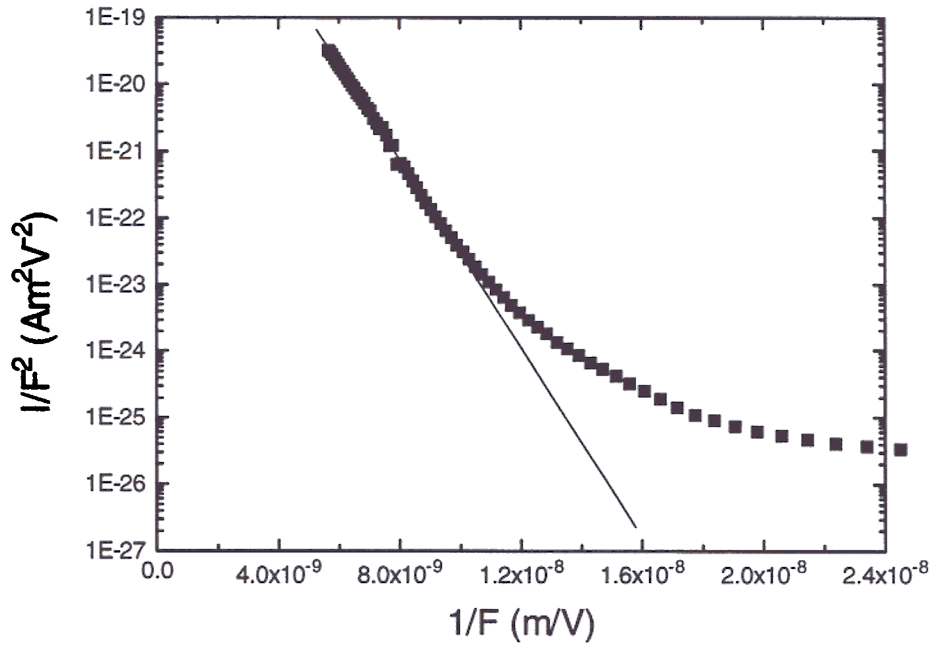
Fig. 4.21: Fowler-Nordheim plot for the ITO/PVK (~104 nm)/Mg:Ag/Ag device. The device area is 2mm×2mm.
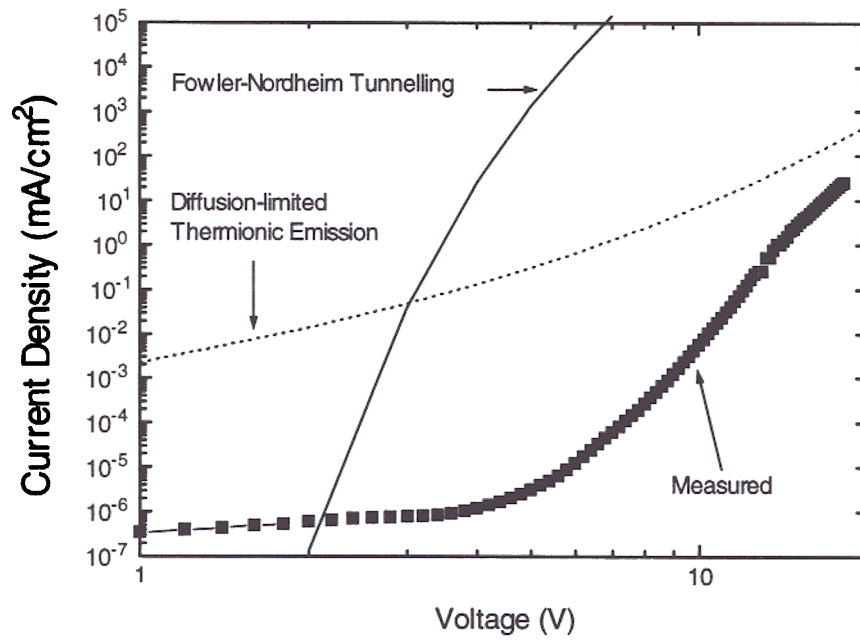
Fig. 4.22: Measured I-V characteristics in comparison with those predicted by Eq. (4.3) and Eq. (4.4). The measured I-V is for the ITO/PVK (~104 nm)/Mg:Ag/Ag device.

enhance the device performance such as the operating voltage by improving the contacts to the same organic materials used in our devices before the limit of the bulk is reached, or by using other methods (e.g. balanced two-carrier injection) to reduce the bulk voltage drop.

4.5.2 Analytical Models for Ideal Two-Carrier Devices

For the general double-carrier injection problem, the governing Poisson and continuity equations become too complicated to be analytically solved (even approximately) because all the carrier traps (two kinds of traps to worry about now!), the recombination and the boundary conditions for non-ohmic contacts have to be taken into account. It makes things even more complicated that the carrier traps in the single-carrier case may behave as recombination centers in the double-carrier case. The only situation where there is an analytical solution is the extremely simple case with double-carrier injection from two ohmic contacts, trap-free transport across the bulk and direct band-to-band recombination of electrons and holes [22]. In this section, we review important results of this analytical model to acquire qualitative understanding of how double-carrier injection affects a device.

In this ideal case, the I-V characteristics have the form of:

$$J = \frac{9}{8} \varepsilon \mu_{eff} \frac{V^2}{L^3} \tag{4.5}$$

where μ_{eff} is an effective carrier mobility. Notice that this form is the same as that of a single-carrier trap-free SCL current, except that the mobility used here is the effective mobility. This effective mobility is a function of the hole mobility μ_p, electron mobility μ_n and recombination rate.

We now examine the implications of this analytical model to qualitatively understand how double-carrier injection affects a device. When the recombination rate

105

constant C_r is small and the electron and hole mobilities are well matched, μ_{eff} can be approximated to be

$$\mu_{eff} = \frac{2}{3}[\frac{4\pi e \mu_n \mu_p (\mu_n + \mu_p)}{\varepsilon C_r}]^{1/2} \qquad (4.6)$$

The physical significance of a small recombination rate is that recombination is not a great hindrance to charge as it moves through the sample Electrons and holes will mix and neutralize the space charge in a wide recombination zone within the sample. This is the case of "injected plasma" and is illustrated in Fig. 4.23(b). The charge neutralization can lead to a significant increase in the current flow, compared to the single-carrier SCL current, because space charge which tend to retard current flow is reduced. If however, the recombination rate is high, the width of the recombination zone will be narrow, as the electrons and holes will have little time to mix before they recombine. In this case, μ_{eff} approximates to

$$\mu_{eff} = \mu_p + \mu_n$$

The schematic charge density profile for this case is shown in Fig. 4.23(a), and the current is simply the sum of two single-carrier SCL currents. Note that compared to the single-carrier SCL current across the same sample thickness, a lower voltage is required for the same current flow in this two-carrier case since holes (or electrons) move a shorter distance If the carrier mobilities are not well matched, so that for instance the hole mobility is much larger than the electron mobility, then

$$\mu_{eff} \approx \mu_p$$

In this case, the current is like a single-carrier SCL current. The electrons are so sluggish that they never get significantly away from the cathode before they recombine with holes. The position of the recombination zone is also determined by the relative mobilities of electrons and holes. It is closer to the contact which injects the less mobile carriers. If
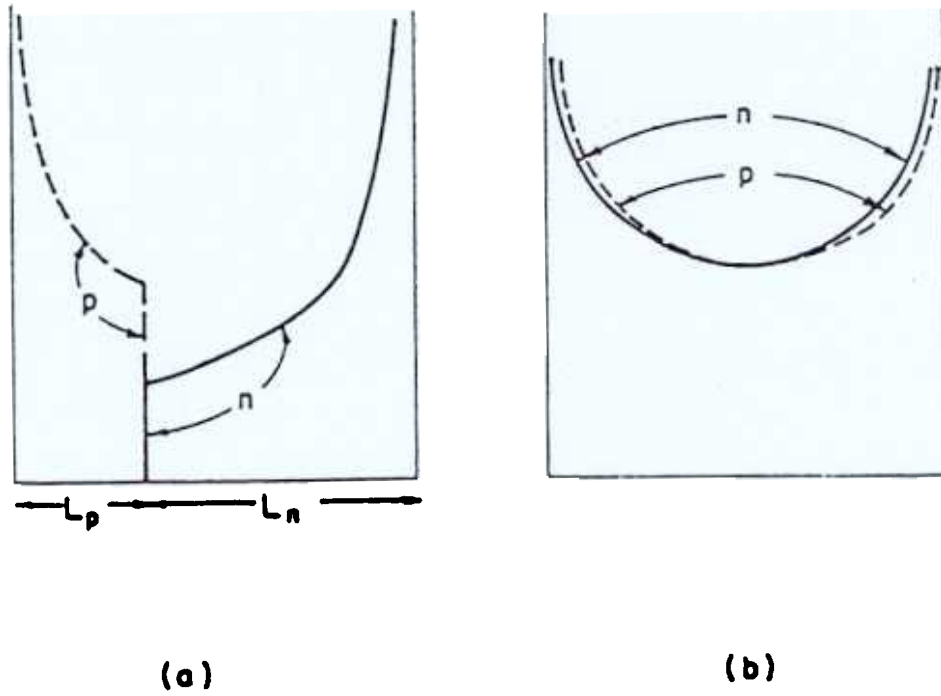
106

(a)   **(b)**

Fig. 4.23: Schematic variation of the injected electron and hole densities, n and p, respectively, for the problem of double injection into a trap-free insulator, for two limiting situations: (a) large recombination rate limit, corresponding to back-to-back, single-carrier SCL currents and (b) small recombination rate limit, corresponding to an injected plasma. (From Ref. [22])

there is a large discrepancy between the mobilities of two species, then the recombination zone will begin at the contact.

The most important implication from this analytical model of the ideal two-carrier device is that balanced carrier injection, balanced carrier transport and a wide recombination zone can result in substantial neutralization of space charge. As a consequence, the current significantly increases in comparison with the single-carrier SCL current at the same voltage in the same material.

4.5.3 Qualitative Model for Doped Polymer Devices

In analyzing our doped polymer devices, we are facing a difficult two-carrier problem: non-ohmic contacts, traps and recombination (although the fabrication of these devices is relatively easy!) Without knowing the analytical form of the I-V characteristics of the non-ideal case, it is difficult to give quantitative analysis of the device characteristics of the single-layer doped polymer OLEDs presented in this chapter. Furthermore, since the contacts to the doped polymer OLEDs are not nearly ohmic, we have the difficulty of separating the contributions from the contact injection or the bulk transport in the device characteristics. A particular case in point is the dependence of device characteristics on the blend composition, since the change of the hole transporter-to-electron transporter ratio affects both the injection and transport properties of both carriers. However, we can make the following qualitative remarks to some details of the device characteristics of the single-layer doped polymer OLEDs.

Fig. 4.24(a) shows the I-V characteristics for the optimized ITO/PVK:PBD:C6 (100:40:0.3 by wt.)/Mg:Ag/Ag devices with different blend thicknesses. All these logI-logV curves have single-carrier TCL-like characteristics. It was also *repeatedly* observed that there is a transition in the curve shape from a thinner device to a thicker device. In a thinner (e.g. ~1050 Å) device, the current does not follow a single power law of voltage (e.g. $I \propto V^{m+}$, m ~12 for lower current levels and m ~6 for higher current levels). In the
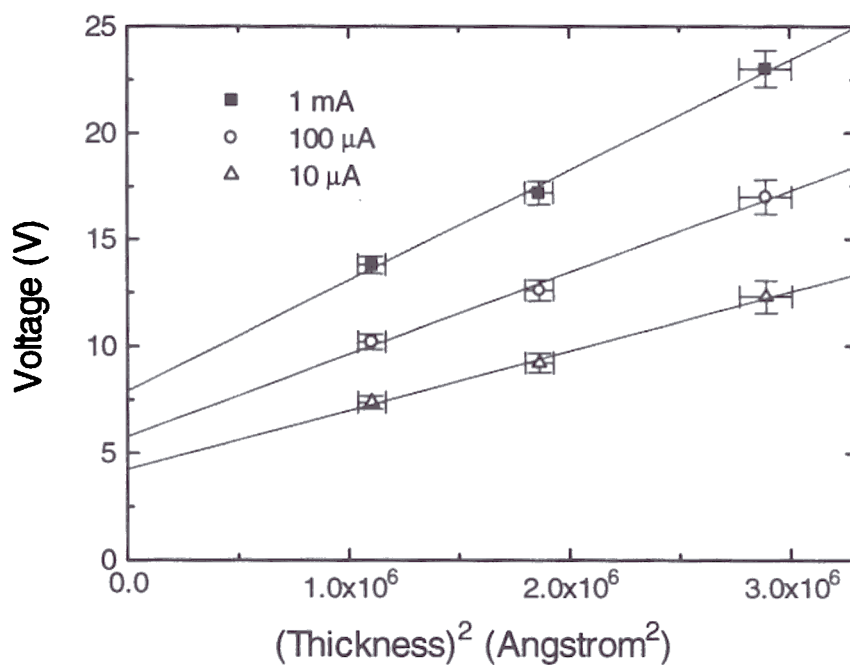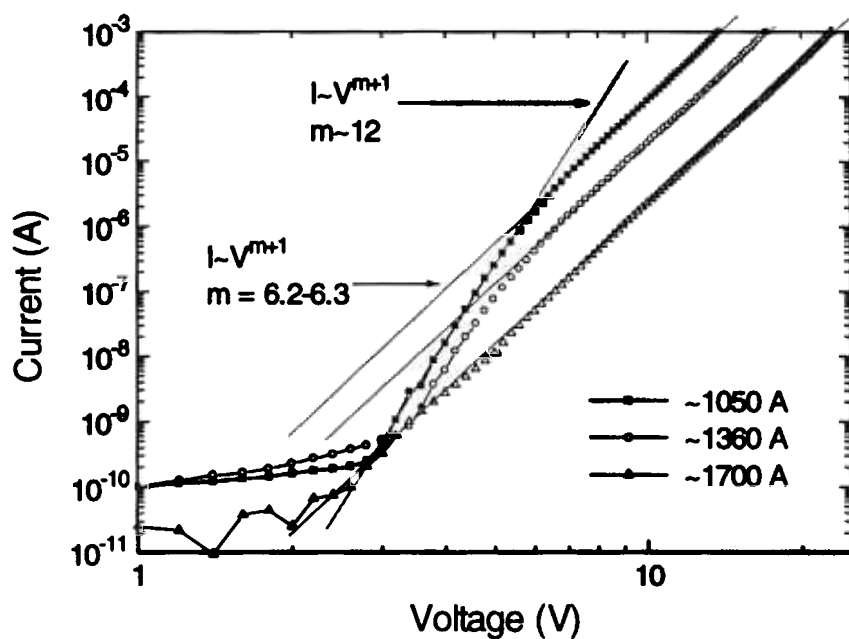
108

Fig. 4.24: (a) Forward I-V characteristics of ITO/PVK:PBD:C6 (100:40:0.3 by wt.%)/Mg:Ag (1200 Å)/Ag (800 Å) devices with different blend thicknesses. (b) V-L^2 plots of Fig. 4.24(a) for different current levels. The device area is 2mm×2mm.

thicker device, the current follows closely a single power law of voltage (m~6) It is not understood whether this is because the thicker device becomes more bulk-limited or because the situation of charge neutralization or carrier recombination varies with the film thickness and the carrier distribution. As in the PVK devices, the linear fits to the V-L^2 for different current levels generate intersection voltages comparable to the full drive voltages (Fig. 4.24(b)). Of course, this fitting only makes sense if the double-carrier TCL current with two ohmic contacts is also proportional to V^{m+1}/L^{2m+1}. To clarify the above questions, further work is necessary.

Since both the injection and bulk properties are important in the doped polymer devices, the dependence of EL on PBD content (Fig. 4.12) probably results from the combination of two effects: improved electron injection and improved electron transport as PBD is added. While improved electron injection improves the balance of carriers, the improved electron transport could move the major recombination zone away from the organic/cathode interface, reducing the metal contact quenching effect. From the discussions in Chapter 2 (section 2.4, Fig. 2.10, Fig. 2.11 and Fig. 2.12), we note that the electron mobility usually increases (rapidly) with increasing PBD concentration in a polymer binder [12], while the hole mobility of PVK could be perturbed (i.e. reduced) by the additives [6-9]. The optimal PVK:PBD ratio for EL could therefore be the tradeoff between hole injection/transport and electron injection/transport. That the lowest drive voltage occurs in the device with the highest quantum efficiency (Fig. 4.13) might be due to a larger extent of charge neutralization within the recombination zone for better balanced carrier injection and transport. There is evidence showing that the recombination zone in a single-layer polymer OLED could be rather broad (i.e. a portion of the film thickness) [27, 32]. When either hole or electron current is dominant, the balance of currents and therefore the extent of charge neutralization may be reduced, leading to a higher voltage and lower EL efficiency. In addition, unbalanced carrier injection/transport

could move the recombination zone closer to the cathode or anode, resulting in luminescence quenching and lower EL efficiency.

These concepts were tested by replacing PBD with BND, another electron-transport oxadiazole molecule which has similar electrochemical properties to PBD (Table 4.1) but has a much higher electron mobility when dispersed in a polymer binder [12] In this case, a stronger effect of electron transporter content on EL efficiency was observed. The comparison of the EL efficiencies of BND and PBD devices is made in Fig 4.25 Although blend compositions are given as the weight ratios, molecular weights of BND and PBD are similar (322.37 vs. 354.46). Though the optimal EL efficiency is about the same for both PBD and BND devices, the BND device is optimized at lower electron transporter content (~20 wt.% of BND vs. ~30 wt.% of PBD in PVK), with a steeper falloff of the EL efficiency away from the optimum. Also, the optimal BND device requires a lower operating voltage than the optimal PBD devices, as shown in Fig. 4.26. We propose that the better electron injection/transport ability of BND leads to a balance of carrier injection/transport at lower BND content, and to steeper rise and falloff of EL efficiencies with BND content Since less BND is required for optimization, the hole injection/transport of PVK may be less perturbed, meaning that both better hole and electron injection/transport contribute to the lower operating voltage of the optimal BND device. The blend devices using BND as an electron transporter, however, were not further explored mainly because they tended to break down at lower current levels than PBD devices and therefore were less stable.

Based on the experimental results and the preceding discussions, how a blend device works is illustrated in Fig. 4.27. Holes are injected and transport through the hole-transport carbazole groups on PVK (hole-transport material, HTM) and electrons are injected and transport through the electron-transport molecules (ETM). From the big difference in the enhancement of photoluminescence and electroluminescence with emitting dopants, it is believed that the gain in electroluminescence is mainly from the
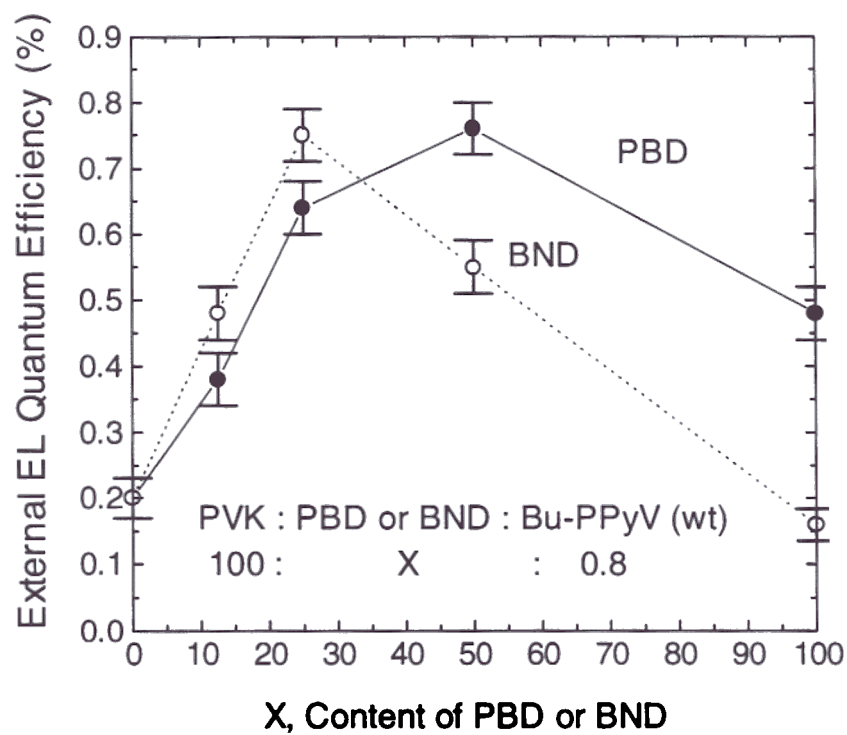
1

Fig. 4.25: External EL efficiency of ITO/PVK:PBD:Bu-PPyV (1050 Å)/Mg:Ag (1200 Å)/Ag (800 Å) devices and ITO/PVK:BND:Bu-PPyV (1050 Å)/Mg:Ag (1200 Å)/Ag (800 Å) devices vs. content of PBD or BND.
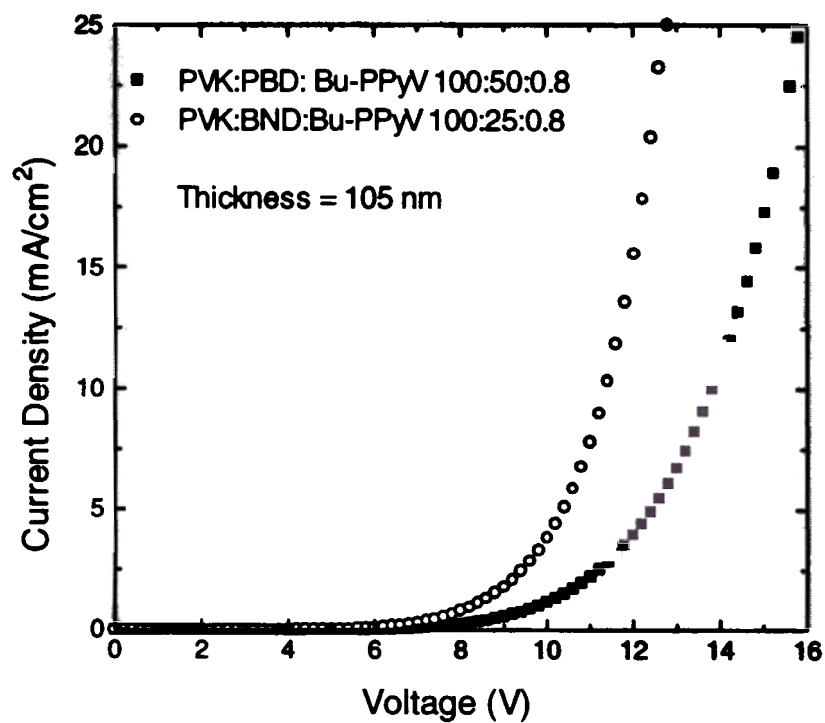
Fig. 4.26: Forward I-V characteristics of optimal ITO/PVK:PBD:Bu-PPyV (1050 Å)/Mg:Ag (1200 Å)/Ag (800 Å) and ITO/PVK:BND:Bu-PPyV (1050 Å)/Mg:Ag (1200 Å)/Ag (800 Å) devices
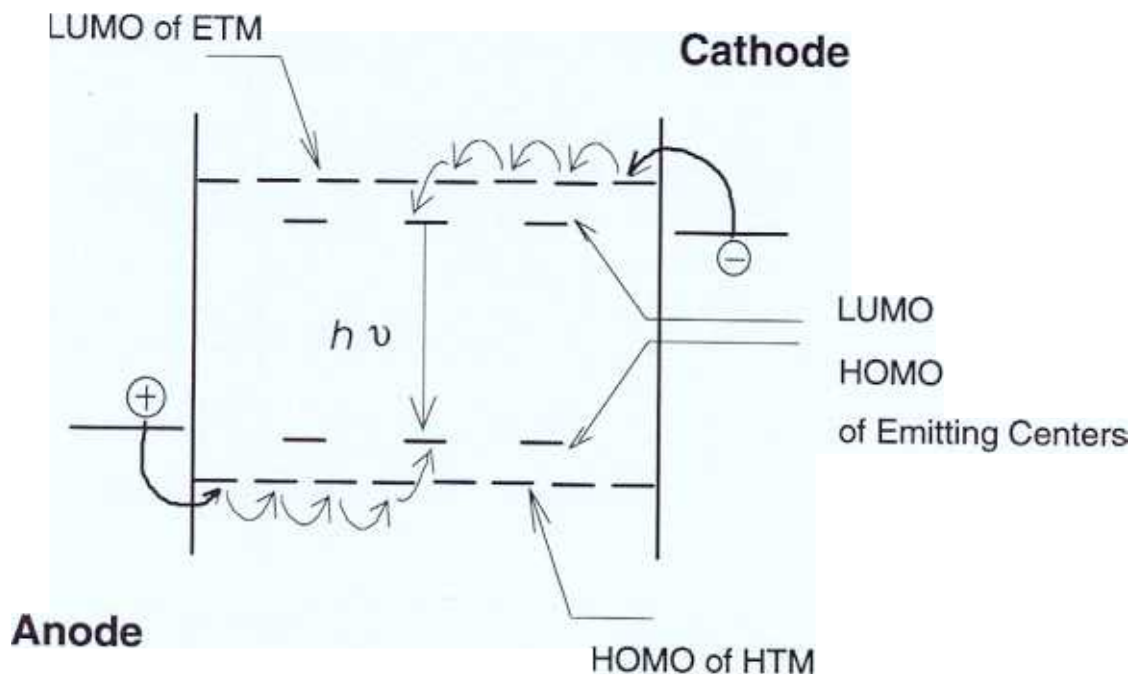
Fig. 4.27: Schematic illustration of the operation of a blend OLED.

enhancement of radiative carrier recombination on the efficient emitting dopants through direct formation of excitons by sequential trapping of oppositely charged carriers. optimization of the quantum efficiency of a blend OLED would require maximizing the overlap between the electron and hole distribution at an optimal location, which is generally desired to be away from both contacts to avoid contact quenching. distributions of electrons and holes, of course, depend on many factors: (i) the relative injection efficiencies of electrons and holes, (ii) the relative transport abilities of electrons and holes, and (iii) the relative characteristics of traps for holes and electrons instance, the dependence of the device performance on the ratio between hole and electron transporters is apparently related to (i) and (ii).

4.6 Summary

Single-layer doped electroluminescent devices based on the hole-transport polymer PVK were studied in detail. From the optical, electrical and electrochemical characterization of materials and devices, it is believed that charge carrier trapping is the mechanism responsible for the large enhancement of EL in both the PVK : fluorescent dopant system and PVK : electron-transport dopant : fluorescent dopant system. Our data support the conclusion that the excitons are formed by sequential capture of electrons and holes at the emitting centers, as opposed to the transfer of excitons from the carrier transporters to the emitting centers. To optimize the EL efficiency and the operating voltage of this class of devices, the addition of electron-transport materials and emitting materials has to be properly adjusted so that the bipolar carrier balance, optimal location of recombination zone and high radiative efficiency of emitting dopants can be achieved. Using appropriate blends, devices with an external EL quantum efficiency >1%, a turn-on voltage of 3V and a drive voltage of ~10V for 100 cd/m^2 can be achieved.

References

[1] J. Tian, C.C.Wu, M.E. Thompson, J.C. Sturm, R.A. Register, M.J. Marsella and T.M. Swager, Adv. Mater. **7**, 395 (1995).

[2] J. Tian, C.C. Wu, M.E. Thompson, J.C. Sturm and R.A. Register, Chem. Mater. **7**, 2190 (1995).

[3] J. Pommerehne, H. Vestweber, W. Guss, R.F. Mahrt, H. Bässler, M. Porsch and J. Daub, Adv. Mater. **7**, 551 (1995).

[4] M.R. Andersson, M. Berggren, O. Inganäs, G. Gustafsson, J.C. Gustafsson-Carlberg, D. Selse, T. Hjertberg and Wennerström, Macromolecules **28**, 7525 (1995).

[5] N.C. Greenham and R.H. Friend, Solid State Physics **49**, 1-148 (1995).

[6] J. Mort and D.M. Pai (ed.), Photoconductivity and Related Phenomena, Elsevier Scientific Publishing Company, 1976

[7] J.A. Chilton and M.T. Goosey, Special Polymers for Electronics and Optoelectronics, Chapman & Hall, 1995

[8] T.A. Skotheim, Handbook of Conducting Polymers, Marcel Dekker Inc., 1986

[9] W.D. Gill, J. Appl. Phys. **43**, 5033 (1972)

[10] V. Choong, Y. Park, Y. Gao, T. Wehrmeister, K. Müllen, B.R. Hsieh and C.W. Appl. Phys. Lett. **69**, 1492 (1996).

[11] S. Saito, T. Tsutsui, M. Era, N. Takada, C. Adachi, Y. Hamada and T. Wakimoto, Proc. SPIE **1910**, 212 (1993).

[12] H. Tokuhisa, M. Era, T. Tsutsui and S. Saito, Appl. Phys. Lett. **66**, 3433 (1995)

[13] C.W. Tang, S.A. VanSlyke and C.H. Chen, J. Appl. Phys. **65**, 3610 (1989)

[14] D.M. Pai, J.F. Yanus and M. Stolka, J. Phys. Chem. **88**, 4714 (1984)

[15] I.D. Parker, Q. Pei and M. Marrocco, Appl. Phys. Lett. **65**, 1272 (1994).

[16] C. Zhang, H. von Seggern, K. Pakbaz, B. Kraabel, H.-W. Schmidt and A.J. Heeger, Synth. Metals, **62**, 35 (1994).

[17] C. Zhang, H. von Seggern, B. Kraabel, H.-W. Schmidt, A.J. Heeger, Synth. Metals, **72**, 185 (1995).

[18] G.E. Johnson, K.M. McGrane and M. Stolka, Pure and Appl. Chem. **67**, 175 (1995).

[19] J. Kido, H. Shionoya and K. Nagai, Appl. Phys. Lett. **67**, 2281 (1995).

[20] C.C. Wu, C.I. Wu, J.C. Sturm and A. Kahn, Appl. Phys. Lett. **70**, 1348 (1997)

[21] K.C. Kao and W. Hwang, Electrical Transport in Solids, Pergamon Press Inc., 1981

[22] M.A. Lampert and P. Mark, Current Injection in Solids, Academic Press, New York, 1970

[23] W. Schottky, Z. Phys. **118**, 539 (1942)

[24] R.H. Fowler and L. Nordheim, Proc. R. Soc. London, Ser. A **119**, 173 (1928)

[25] P.E. Burrows, Z. Shen, V. Bulovic, D.M. McCarty, S.R. Forrest, J.A. Cronin and M.E. Thompson, J. Appl. Phys. **79**, 7991 (1996)

[26] P.W.M. Blom, M.J.M. de Jong and J.J.M. Vleggaar, Appl. Phys. Lett. **68**, 3308 (1996)

[27] P.W.M. Blom, M.J.M. de Jong and C.T.H.F. Liedenbaum, IEDM TEch. Dig., 571 (1995)

[28] C. Hosokawa, N. Kawasaki, S. Sakamoto and T. Kusumoto, Appl. Phys. Lett. **61**, 2503 (1992)

[29] H. Antoniades, M.A. Abkowitz and B.R. Hsieh, Appl. Phys. Lett. **65**, 2030 (1994)

[30] I.D. Parker, J. Appl. Phys. **75**, 1657 (1994)

[31] C.R. Crowell and S.M. Sze, Solid State Electron. **9**, 1035 (1966)

[32] U. Lemmer, D. Vacar, D. Moses, A.J. Heeger, T. Ohnishi and T. Noguchi, Appl. Phys. Lett. **68**, 3007 (1996)

Contacts to Single-Layer Doped Polymer LEDs

5.1 ITO Anode Contacts

5.1.1 Introduction to ITO

Indium tin oxide (ITO) belongs to a class of materials, transparent conducting oxides (TCO), which are non-stoichiometric and doped films of oxides. These materials exhibit high transmittance for visible light and nearly metallic conductivity. These transparent conductors have found many applications, ranging from window heaters to active optoelectronics. Because of its fairly good efficiency as a hole injector into organic materials, ITO has also been widely used as the anode contact for OLEDs.

Indium tin oxide is tin-doped indium oxide (In_2O_3). In_2O_3 is a wide band gap semiconductor, with a band gap about 3.5 eV. This large band gap is the reason why it is transparent. During the deposition of indium oxide, structural defects such as oxygen vacancies V_O are introduced into the film. Oxygen vacancies could cause shallow donor states just below the conduction band edge. If the concentration of oxygen vacancies is high, they form an V_O impurity band which overlaps the conduction band edge E_c at the bottom of the conduction band, producing a degenerate semiconductor [1,2], as illustrated in Fig. 5.1. Indium oxide can be further heavily doped n-type by the substitution of Sn for In. Therefore, ITO is a degenerate n-type semiconductor with both substitutional Sn

dopants and structural defects contributing to the high carrier (electron) concentration and with the Fermi level E_F above E_c. The carrier concentration, usually in the range of 10^{20}-10^{21} /cm^3, provides for high conductivity. Fig. 5.2 shows typical transmittance, reflectance and absorptance spectra for an ITO film [2]. The visible and near-IR regions are the transparent regions. In the near-IR region, the free-carrier absorption becomes important and can be explained by classical Drude theory. The absorption peak is due to the plasma resonance. For wavelengths larger than the plasma wavelength, the plasma becomes reflective, explaining the highly reflecting IR region. Due to its high reflectance in IR region, ITO is used as a heat mirror in some applications.

Conduction Band

Ec

E_F

$\}$ Vo + Sn dopants
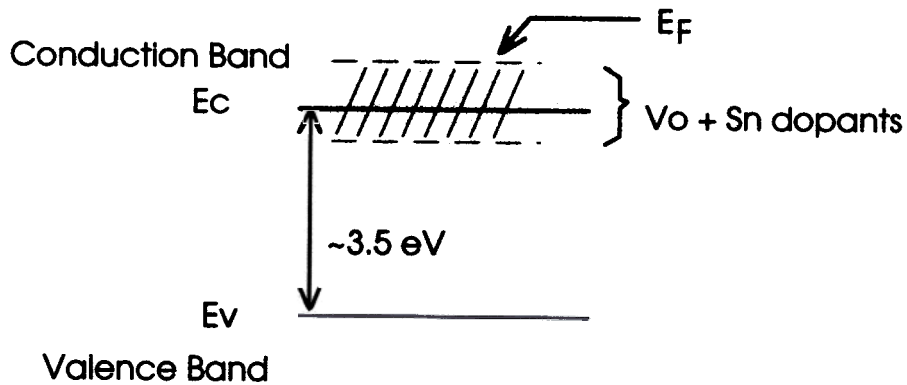
~3.5 eV

Ev

Valence Band

Fig. 5.1: Schematic band model for indium tin oxide.

Various thin film deposition techniques have been used to deposit ITO, including evaporation, sputtering, chemical vapor deposition (CVD) and even dip-coating from a solution containing metal compounds followed by heat treatment. Among them, sputtering is most widely used. ITO could be deposited by reactive sputtering from the In:Sn alloy in a sputtering gas containing oxygen. However, sputtering from an In$_2$O$_3$:SnO$_2$ mixed oxide target is more widely used due to better control of stoichiometry of the resulting films. Because of the dissociation of oxygen during sputtering, a small
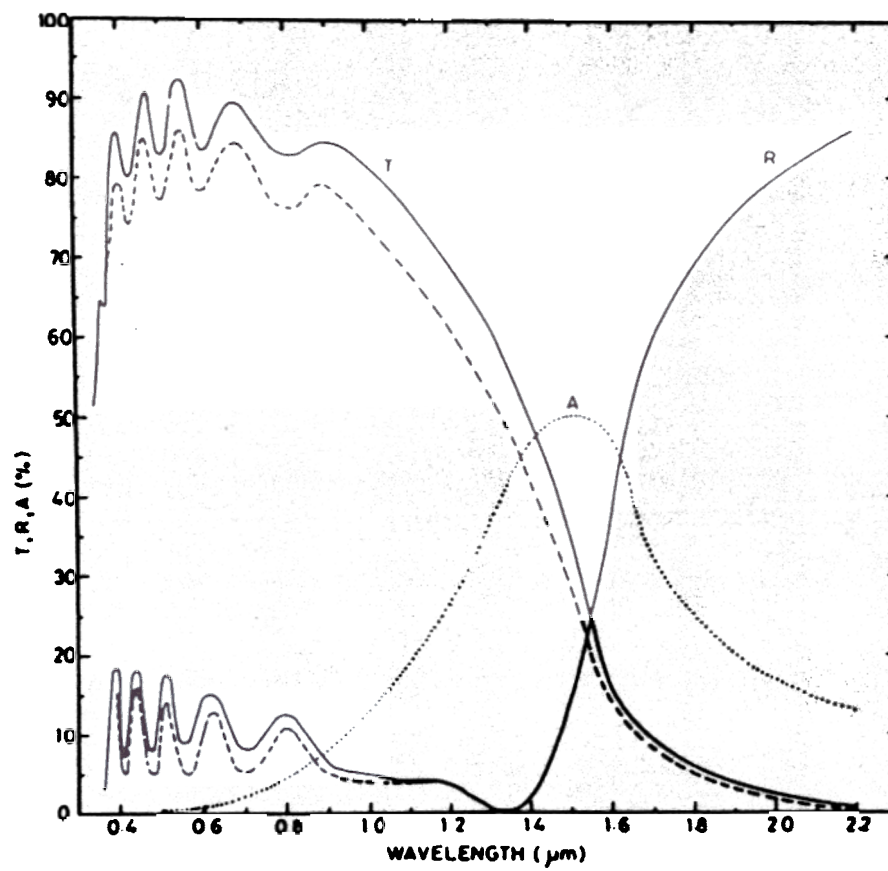
Fig. 5.2: Typical reflectance R, transmittance T and the absorptance A spectra of an ITO film. (from Ref. [2])

120

oxygen partial pressure in the sputtering gas such as Ar is necessary to control the oxygen vacancies for the optimal properties. Heat treatment between 150 °C and 500 °C during or after film deposition is also normally required for better properties. Films undergoing heat treatment usually are polycrystalline and have larger grain sizes, fewer structural defects and therefore higher electron mobilities.

Since the organic thin film is in direct contact with the ITO in the OLEDs, the surface properties of the ITO are expected to directly affect the characteristics of the device. Abnormal device behavior such as shorting, unstable I-V characteristics and damage on the surface of the top cathode contact and organic thin films after continuous operation of devices have been observed in OLEDs built on bare, cleaned ITO surfaces [3-5]. Furthermore, as-grown ITO contacts have been found to be less efficient for hole injection than low work function metal cathodes for electron injection, resulting into hole-limited devices [6,7]. The mitigation of these problems has so far involved modifying the structures and properties of the organic materials or introducing an intermediate stabilization/barrier layer with proper carrier injection/transport characteristics between the ITO and the active luminescent layers [7,8]. The alternative of modifying the ITO itself, however, has not been extensively investigated. In this section, the effects of various treatments of ITO on the properties of ITO itself and device characteristics are discussed. It is demonstrated that proper surface modification leads to improvements in single-layer polymer-based OLEDs, where the ITO surface properties are more critical than in multilayer devices.

5.1.2 Effects of Various ITO Treatments on OLEDs

Prior to their use, the ITO-coated glass substrates were cleaned as described in Chapter 3. The substrates were then used as cleaned or treated by either UV-ozone [8,9] or a plasma before deposition of the organic layer. The UV-ozone treatment was carried out in the UV-ozone cleaning system (T10X10/OES, UVOCS Inc.). UV emission in the

254 nm and 185 nm range is generated by low pressure quartz-mercury vapor lamps with a 254 nm UV intensity of ~10 mW/cm^2 at a distance of one inch from the lamps. The 185 nm radiation is absorbed by atmospheric oxygen, changing it to ozone and atomic oxygen. For the plasma treatment, the ITO samples were exposed to plasmas of different gases under various conditions in a parallel-plate type plasma reactor (RIE-80, Plasma Technology Inc.) configured in the reactive ion etching (RIE) mode. In this system, a RF power of 25W corresponds to a power density of ~50 mW/cm^2. All the ITO treatments were carried out at room temperature.

The OLEDs tested in this study are single-layer doped polymer devices, in which blends of PVK:PBD:coumarin 6 (C6) (100:40:0.3 by weight) are used for green devices and PVK:Alq:nile red (100:40:0.2 by weight) for orange-red devices. The organic film thickness was ~1050 Å. At 25 mA/cm^2, the variation of device drive voltage due to variations in blend film thickness was within ±0.25V. This difference is much smaller than the effect of different ITO treatments as will be shown below. After spin-coating, metal cathode contacts consisting of 1200 Å Mg:Ag alloy and 800 Å Ag were deposited through a shadow mask with an array of 2mm×2mm holes.

Fig. 5.3 shows I-V characteristics for devices built on ITO treated in different ways. Fig. 5.4(a) and Fig. 5.4(b) show corresponding brightness-current (L-I) and brightness-voltage (L-V) characteristics. Except for the hydrogen plasma treatment, treatment is optimized for OLED performance by varying exposure time and power. In Fig. 5.3, all forward I-V curves exhibit two regimes, a low-current regime with a weaker voltage dependence and a high-current regime with a steeper current rise with voltage. In all cases, the forward-bias low-current regime, henceforth referred to as "leakage", is always symmetrical to its reverse-bias counterpart. Light emission is observed only in the high-current regime, which we will refer to as the "bipolar" regime. The various ITO treatments affect considerably the turn-on voltage of the "bipolar" current, the "leakage' current, the forward-to-reverse bias rectification ratio, and the quantum efficiency of light
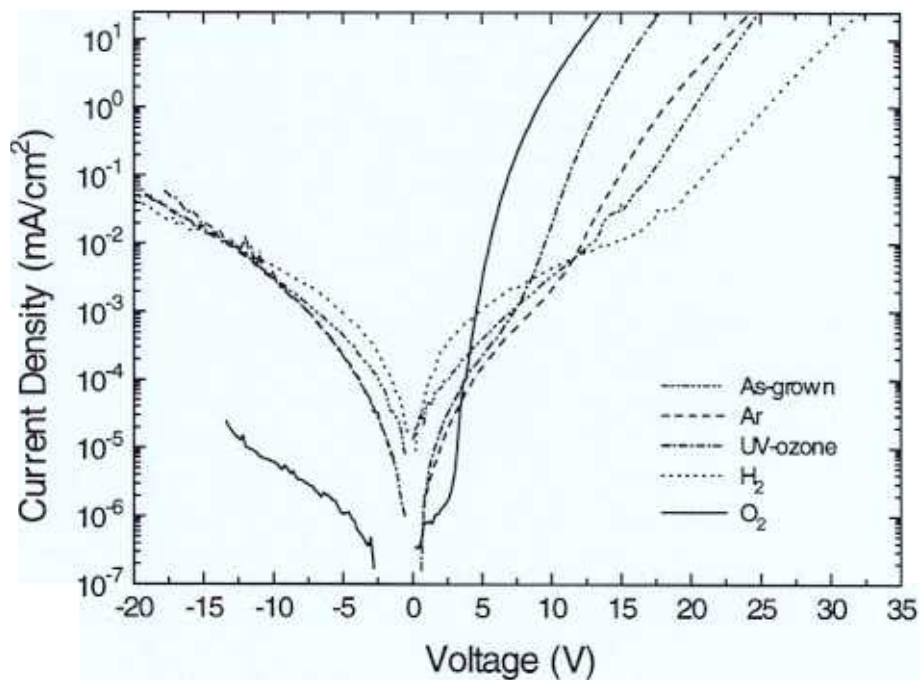
Fig. 5.3: I-V characteristics of OLEDs built on ITO treated in different ways. The device structure is Ag(800Å)/ Mg:Ag(1200Å) /PVK:PBD:C6 (100:40:0.3 by wt., 1050Å)/ITO. ITO treatment conditions: UV-ozone: 3 min.; Ar plasma: 150 mTorr, 25 sccm, 25W, 3 min.; H_2 plasma: 60 mTorr, 25 sccm, 20W, 30 sec.; O_2 plasma: 150 mTorr, 25 sccm, 25W, 4 min.
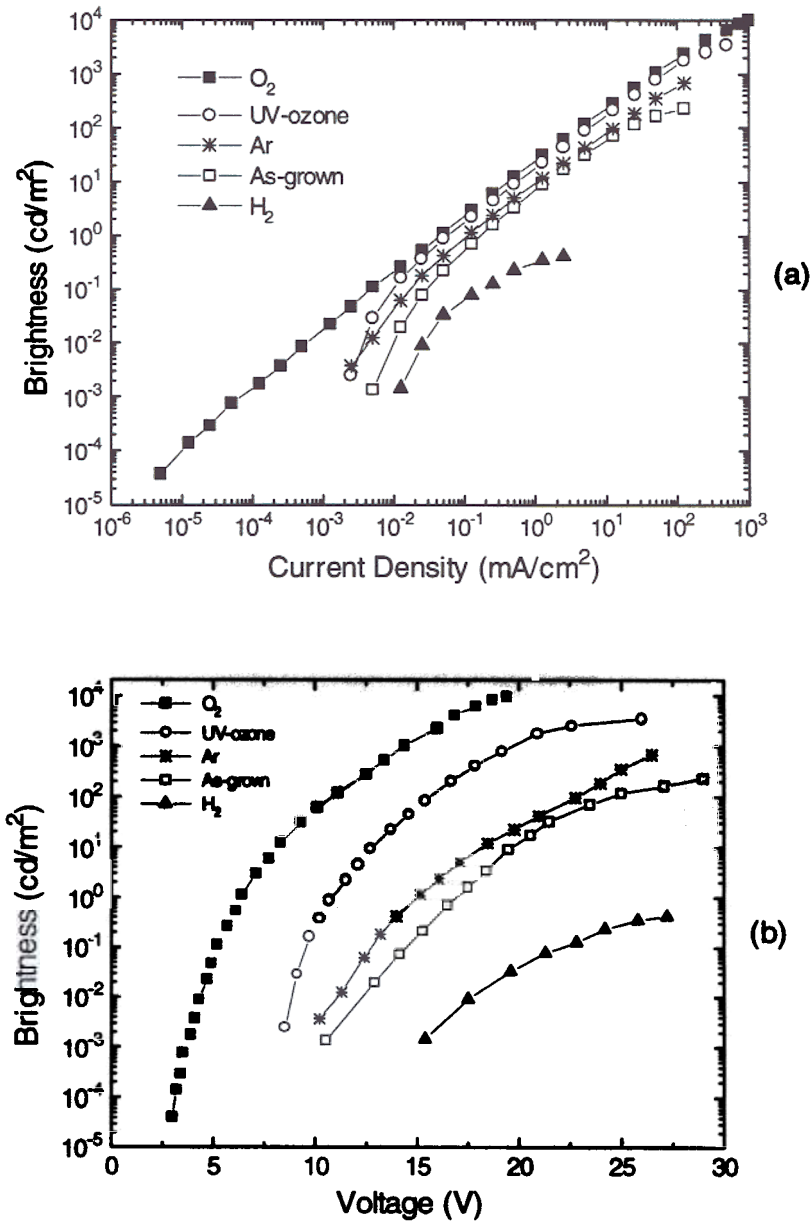
Fig. 5.4: (a) brightness vs. current and (b) brightness vs. voltage of OLEDs built on ITO treated in different ways. The device structure and ITO treatment conditions are the same as listed in **Fig. 5.3**.

emission. Devices made on cleaned "as-grown" ITO have a turn-on voltage of ~12V and an external quantum efficiency at 2.5 mA/cm^2 of 0.28% photon/electron. The Ar plasma treatment (25W, 3 min.) slightly reduces the turn-on to 11V and increases the efficiency to 0.35%. The optimal UV-ozone treatment (~3 min.) improves these parameters to 8V and 0.7%, respectively. Most important, the oxygen plasma treatment (25W, 4 min.) dramatically reduces the turn-on voltage to 3V and brings the efficiency to 1%. In addition, the oxygen plasma treatment substantially suppresses the reverse current and greatly increases the rectification ratio (at the voltage for a 25 mA/cm^2 forward current) from ~100 to ~10^6, resulting in a highly rectifying diode. The hydrogen plasma treatment (20W, 60 mtorr, 30 sec.), on the other hand, increases the turn-on to 17V and reduces the efficiency to 0.007%. In devices made on the hydrogen plasma-treated ITO, local sparks appear across the contact surface at current densities as low as 2.5 mA/cm^2 and quickly lead to open-circuited devices. In devices made on as-grown and Ar plasma-treated ITO, devices break down around 100 mA/cm^2. In contrast, devices made on oxygen plasma-treated ITO can sustain currents as high as 1000 mA/cm^2 to achieve a maximum brightness of ~10,000 cd/m^2 around 19V before the sparks appear and rapid device deterioration occurs. Table 5.1 below summarizes the changes in device characteristics brought by various ITO treatments:

	Turn-on Voltage (V)	η_{ext}	Breakdown Current (mA/cm^2)	Max. Brightness (cd/m^2)
As-grown	12	0.28%	~100	~400
Ar	11	0.35%	~100	~700
O$_2$	3	1.0%	~1000	~10,000
UV-ozone	8	0.7%	~500	~3,500
H$_2$	17	0.007%	~3	~0.5

Table 5.1: Summary of effects of various ITO treatments on device characteristics.

In all cases, the forward-bias low-current regime is always symmetrical with its reverse-bias counterpart. Its bias-polarity independence excludes the barrier-controlled mechanism, since barriers for both carriers would be very different between forward bias and reverse bias. A simple ohmic current due to intrinsic carriers in organic films can not explain the variation of these currents by several orders of magnitude for differently treated ITOs. Instead, the large variation is similar to the leakage current at low bias in a non-ideal conventional semiconductor diode. The large variation of this "leakage" current may be related to the reaction or chemistry between the ITO surface and the organic layer. For instance, the oxygen plasma treatment of the ITO surface may help the formation of a thin doped polymer layer with fewer defects. Light emission is observed only in the forward-bias high-current regime and always becomes detectable near the turning point from the low-current regime to the high-current regime. Both the forward low-current regime and reverse bias do not contribute to EL, no matter how large the current is. It seems that the current at all bias levels is actually the combination of two components: one which is actually injected into the bulk of the organic layer and contributes to EL, and the other which is either leakage current or from some other origin and does not contribute to EL. We therefore refer to the forward-bias low-current regime as the "leakage" regime, and the forward high-current regime as the "bipolar" regime. The current at all forwad bias levels is the combination of the "leakage" current and the "bipolar" current, and the turn-on of the "bipolar" current is where the the "bipolar" current starts overwhelming the "leakage" current.

One can easily understand the importance of higher quantum efficiency and lower drive voltage, but the significance of suppressing the reverse current and enhancing the forward-to-reverse bias rectification ratio might not be obvious, because one might think the OLED would be run only in forward bias and the reverse current would not matter. However, if the OLEDs are to be used in a passive-matrix LED display array, then one has to increase the rectification and reduce the reverse current of the OLEDs. Otherwise, the

OLEDs in the active row could cross-talk to neighboring OLEDs through the reverse leakage current, prohibiting the array from functioning normally.

Fig. 5.5(a) and Fig. 5.5(b) shows the I-V and L-I characteristics of OLEDs made on ITO treated by oxygen plasma with higher RF power or longer exposure time, compared to the optimal condition. With long exposure time or high RF power, the turn-on of the "bipolar" regime is not changed but the voltage at higher current levels shifts to higher values. The L-I curves of all nearly superimpose with the external quantum efficiency ~1%. The nearly constant efficiency suggests that the hole injection efficiency is not affected by further oxygen plasma treatment, but that there is a larger voltage drop occurs across the ITO/organic interface or a series resistance on the ITO side, as if there was a series "contact resistance". This series "contact resistance" depends on the oxygen treatment conditions.

Both the UV-ozone and oxygen plasma are oxidizing, but it is interesting to note that the UV-ozone treatment is not as effective as the oxygen plasma treatment in improving the device performance. In addition, the device characteristics are not improved further with an even longer UV-ozone treatment time. It is clear that the UV-ozone treatment is not the same as oxygen plasma treatment, indicating that the oxygen plasma treatment does more than clean the ITO surface. There is some reaction between the oxygen plasma and the ITO that the UV-ozone does not have.

The poor performance induced by hydrogen plasma is reversible and nearly optimal performance can be recovered with a subsequent oxygen plasma treatment. Fig. 5.6 shows the I-V characteristics of OLEDs made on ITO treated by hydrogen plasma (20W, 60 mtorr, 30 sec.) and subsequent oxygen plasma treatment, in comparison with devices built on ITO treated by either oxygen plasma or hydrogen plasma. The strongly oxidizing and reducing natures of the oxygen and hydrogen plasmas suggests an electrochemical oxidation-reduction mechanism.
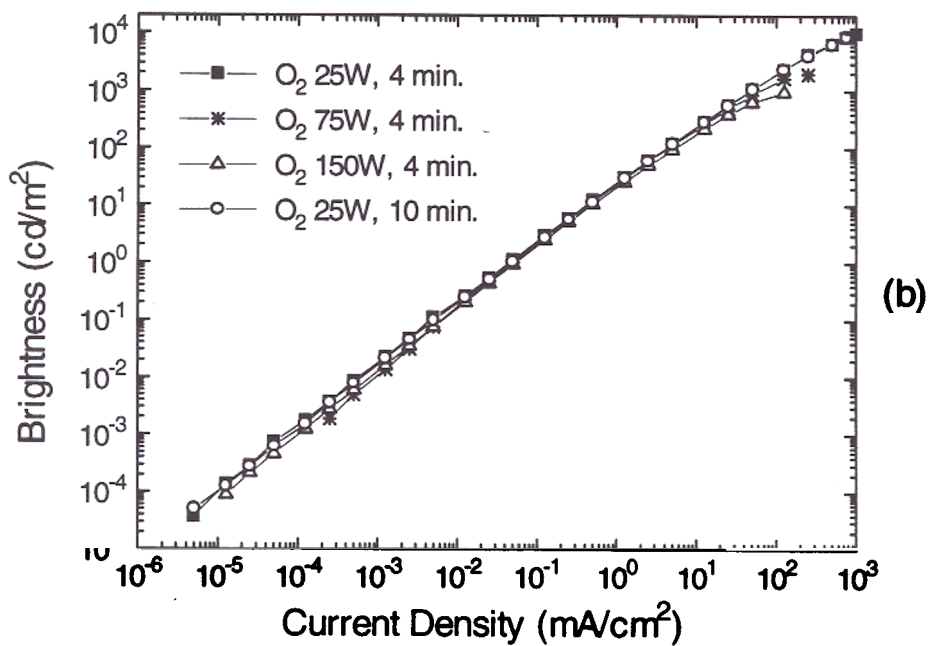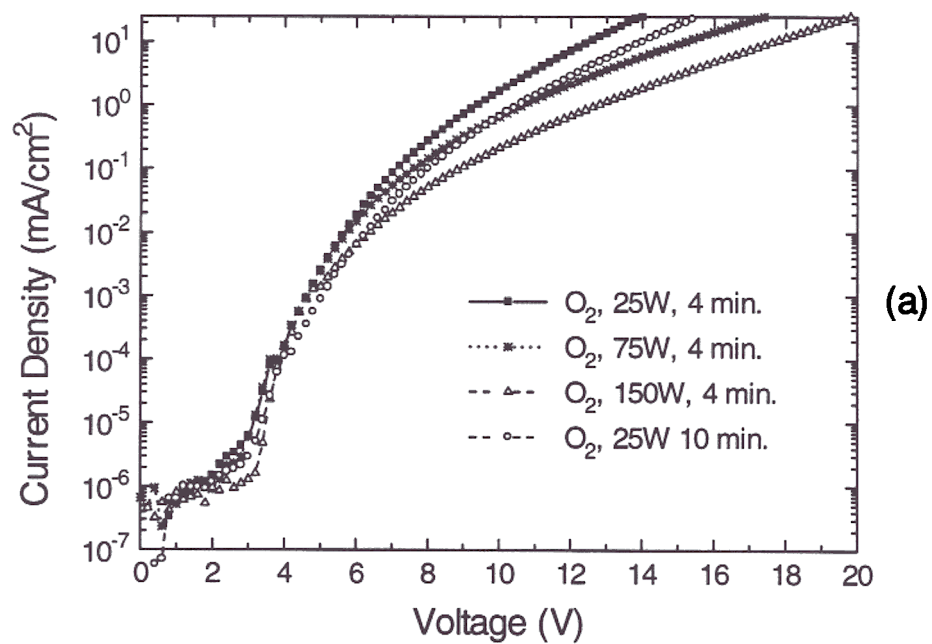
Fig. 5.5: (a) I-V and (b) L-I characteristics of OLEDs built on ITO treated in different oxygen plasma conditions: 150 mtorr, 25 sccm, different RF power, different time.
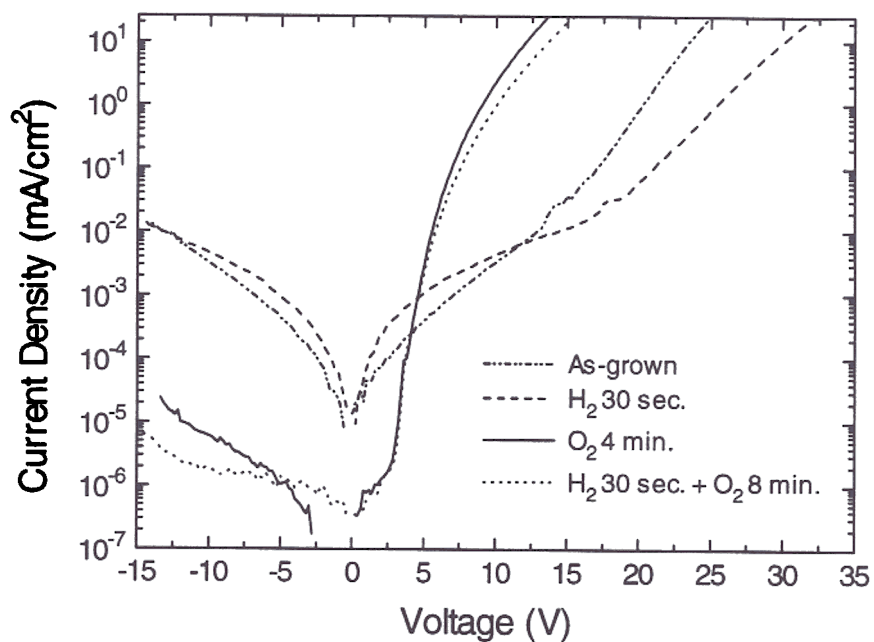
128

Fig. 5.6: I-V characteristics of OLEDs made on ITO treated by hydrogen plasma (20W, 60 mTorr, 30 sec.) and subsequent oxygen plasma treatment (25W, 150 mTorr), in comparison with devices built on ITO treated by either oxygen plasma or hydrogen plasma.

5.1.3 Characterization of ITO

The sheet resistances of ITO before and after certain treatments were measured and they all have the same value (~11 Ω/square). The transmittance of ITO before and after certain treatments were also measured and are shown in Fig. 5.7. Similarly, hardly any change in the transmittance was observed. We therefore conclude that the bulk properties of the ITO are not changed by these treatments, and that the changes in device performance are related to the ITO surface properties.

Previous studies of the degradation of ITO under severe hydrogen or other reducing gas plasma conditions, i.e. long exposure time (minutes), high temperature (100-500 °C) and high power (hundreds of mW/cm^2) [10-14] have shown a large reduction in transmittance, increase in sheet resistance, substantial changes in surface morphology due to the formation of In-rich hillocks, and large nonuniformity of surface compositions due to segregation and coalescence of In-rich clusters [14]. To know how the ITO surface is modified within our experiment conditions, a few techniques were used to probe the surface properties of ITO. These include: (i) atomic force microscopy (AFM) for surface morphology, (ii) Auger electron spectroscopy (AES) for surface chemical compositions, and (iii) ultra-violet photoemission spectroscopy (UPS) for surface work functions. AES and UPS were measured in collaboration with Prof. A. Kahn and C. I. Wu.

Fig. 5.8 shows the 300 nm × 300 nm AFM images of three ITO surfaces probed on the Nanoscope III of Digital Instrument Inc. in the Princeton Material Institute under tapping mode using a Si cantilever. These three ITO samples are cleaned as-grown ITO, oxygen plasma-treated ITO (25W, 25 sccm, 150 mTorr, 4 minutes), and hydrogen plasma-treated ITO (20W, 25 sccm, 60 mTorr) respectively. The grains of ITO can be clearly seen in these images and the grain size is about 20-40 nm. The RMS surface roughnesses for the as-grown, oxygen plasma-treated and hydrogen plasma-treated ITO are 1.6±0.3 nm, 1.4±0.3 nm, and 1.8±0.3 nm, respectively. From both the AFM images and the values of RMS roughness, it is clear that the impact of these treatments on surface
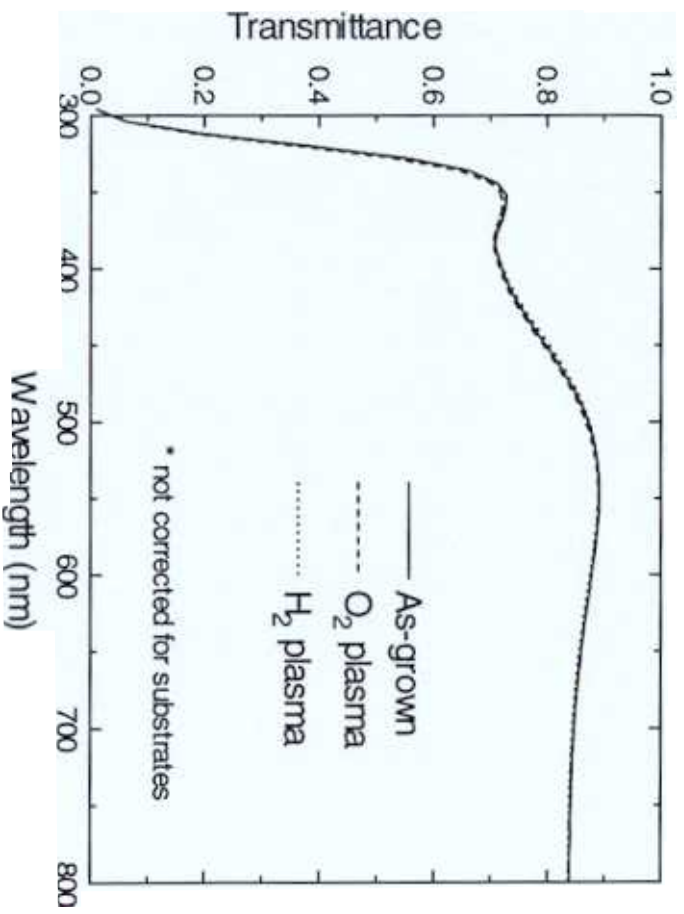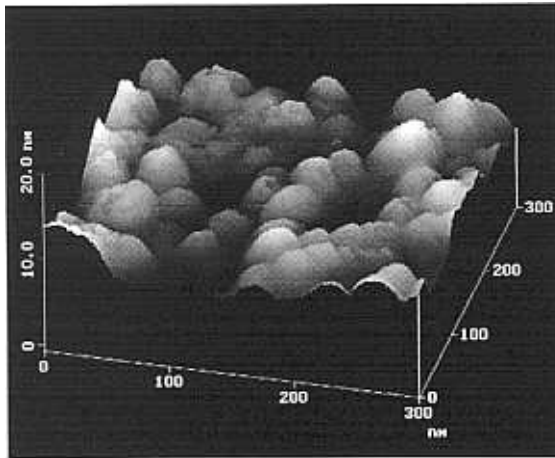
Fig. 5.7: Transmittance spectra of ITO treated in different ways: oxygen plasma: 25W, 150 mtorr, 4 min.; hydrogen plasma: 20W, 60 mtorr, 30 sec.
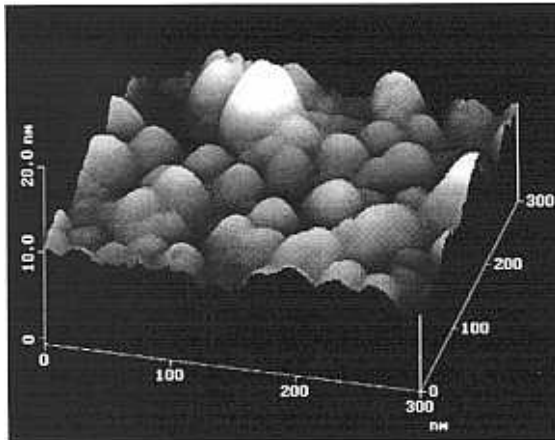
AFM   300 nm × 300 nm
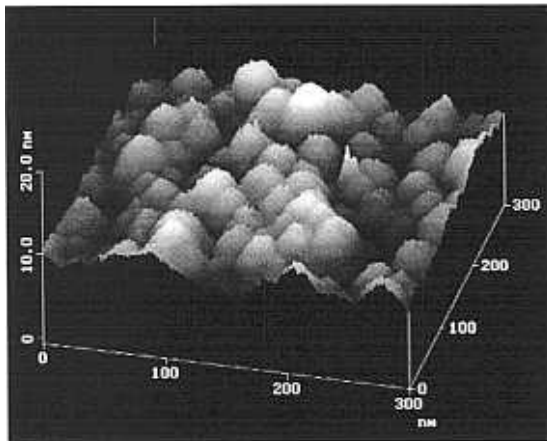

as-grown

grain size:
  20-50 nm
RMS roughness:
  1.6 ± 0.3 nm

O_2 plasma

RMS roughness:
  1.4 ± 0.3 nm

H_2 plasma

RMS roughness:
  1.8 ± 0.3 nm

Fig. 5.8: AFM surface images of the ITO treated in different ways.

morphology is not significant, even though one might expect to see large morphology changes in hydrogen plasma-treated samples as in the previous literature. It is not seen here mainly due to the milder plasma conditions used (room temperature, ~50 mW/cm^2, ~tens of seconds, plasma potentials of ~80-100V).

The chemical profiles of the ITO surface layers were measured by AES with 1 KeV Ar sputtering. The sputtering speed was on the order of a few Å to 10 Å per minute. The AES spectra were taken at one minute intervals with the Ar sputtering turned off. The resulting chemical composition profiles vs. sputtering time for In, Sn and O in various ITO samples are shown in Fig. 5.9. First, all these profiles converge to the same bulk values within a few minutes, confirming that only thin surface layers were changed by the treatments. Secondly, it is seen that the as-grown ITO is rich in Sn and deficient in In near the surface, compared to the bulk. The Sn:In atomic ratio near the surface is almost as high as 1:3, while it is only about 1:10 in the bulk. It has been known that ITO films having good optical and transport properties tend to have relatively Sn-rich surface layers due to the migration of Sn-rich phases to the surface during annealing [1]. The oxygen plasma treatment reduces the Sn concentration and increases the In concentration. The change in Sn:In ratio is dependent on the degree of oxygen plasma treatment. The 25W, 4 minute treatment lowers the surface Sn:In ratio to 1:6 and 150W, 4 minute treatment leads to an even lower Sn:In ratio than the bulk. These composition profiles may be correlated with the differences in device characteristics shown in Fig. 5.5, where ITO treated with oxygen plasma of higher RF power shows a larger "contact resistance". The oxygen plasma treatment also raises the oxygen concentration near the surface, although less significantly. The lack of substantial increase of oxygen concentration is probably due to a self-limited oxygen incorporation process [1]. The oxygen vacancies in the Sn-doped In$_2$O$_3$ allow O^{2-} ion conduction, and this conduction decreases as the number of vacancies decreases. It is possible that during the oxygen plasma treatment, the number of oxygen vacancies decreases, hampering further oxidation into the bulk. This is actually the same
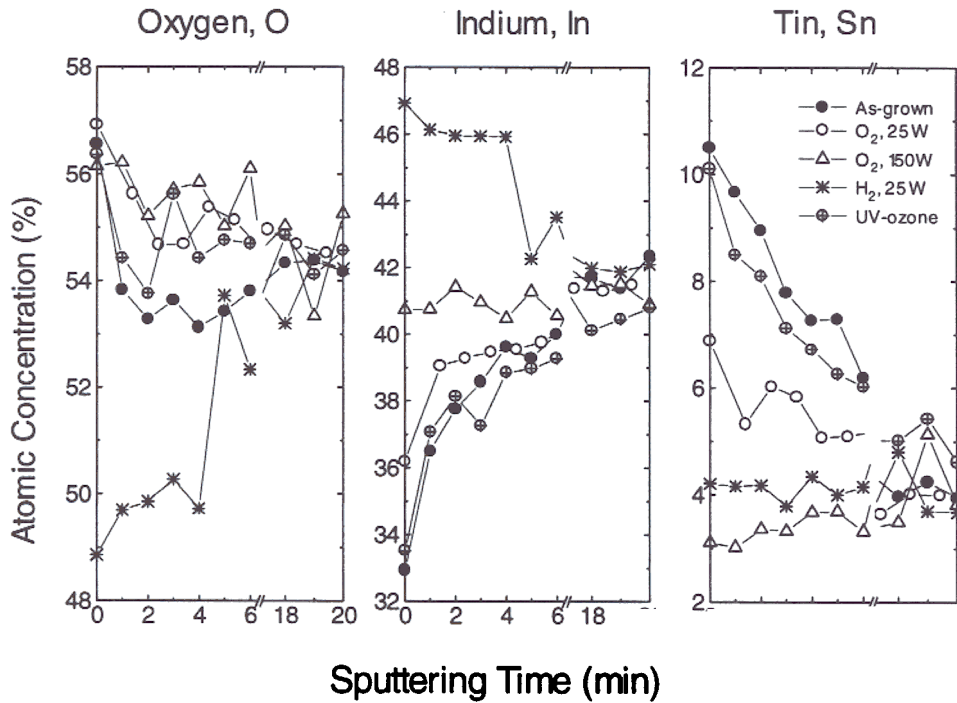
133

Fig. 5.9: (a) O, (b) In and (c) Sn atomic concentration profiles vs. 1 keV Ar sputtering time for ITO treated in different ways. ITO treatment conditions: H_2 plasma: 150 mTorr, 25 sccm, 25W, 3 min.; O_2 plasma: 150 mTorr, 25 sccm, 25W or 150W, 4 min.; clean as-grown ITO; UV-ozone: 3 min.

mechanism which leads to the long-term stability of ITO in ambient conditions. Compared to the oxygen plasma-treated ITO, the UV-ozone treatment hardly changes the Sn or In concentration, clearly indicating that the two treatments are different, consistent with the difference in device characteristics shown in Fig. 5.3 and Fig. 5.4. The hydrogen plasma treatment also reduces Sn surface atomic concentration, but substantially depletes the surface oxygen concentration. This is strong evidence for an electrochemical reduction-oxidation mechanism near the ITO surface in the reducing hydrogen plasma and oxidizing oxygen plasma, respectively. This reduction-oxidation mechanism of the ITO surface is, to some degree, a reversible process, as manifested by the fact that the poor performance caused by a light hydrogen plasma treatment can be cured with a subsequent oxygen plasma treatment of ITO.

The lack of significant changes in surface morphology with different treatments indicates that, within the conditions used, morphology is not the determining factor in the variation observed in device performance. However, the improvement of device performance with oxygen plasma suggests that the surface chemical composition might play a role in increasing the hole injection ability at the ITO/organic interface. The enhancement of hole injection may be due to an increase in the work function of the ITO. To further explore this point, UPS has been carried out to determine the work functions at the surfaces of various ITO samples. He I with the photon energy of 21.22 eV is used as the UV light source. The principle of UPS is schematically illustrated in Fig. 5.10(a) and the general shape of the UPS spectra for ITO smaples are shown in Fig. 5.10(b). In Fig. 5.10(c), the portions of the UPS spectra around the onset and the Fermi level are blown up for ITOs treated in different ways. Since all samples are electrically connected to the system, the Fermi levels of all samples are at the same energy position and the shift of work function is actually reflected in the shift of the onset energy. Compared to the as-grown ITO, the oxygen plasma treatment increases the work function by ~100 meV in the
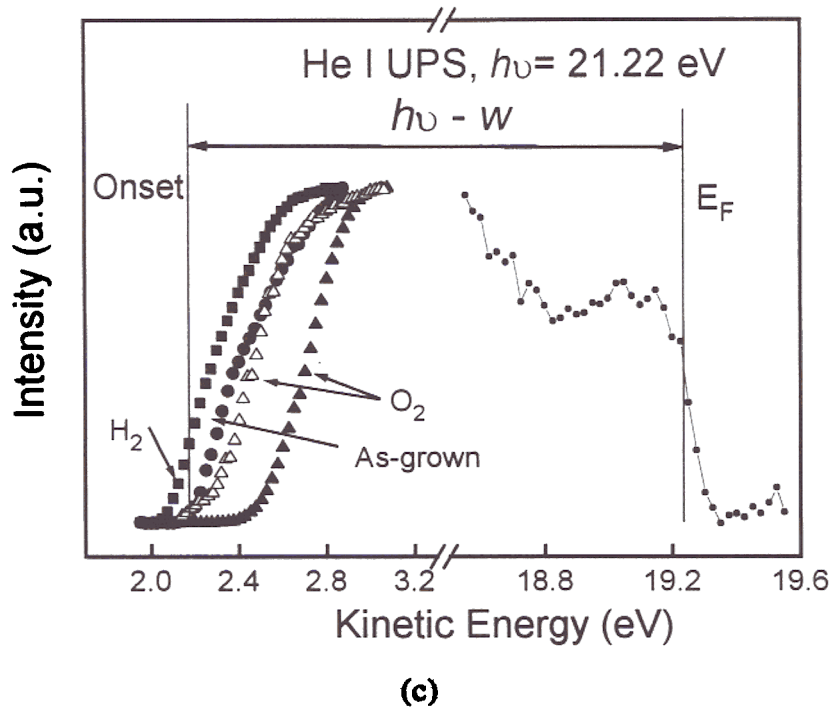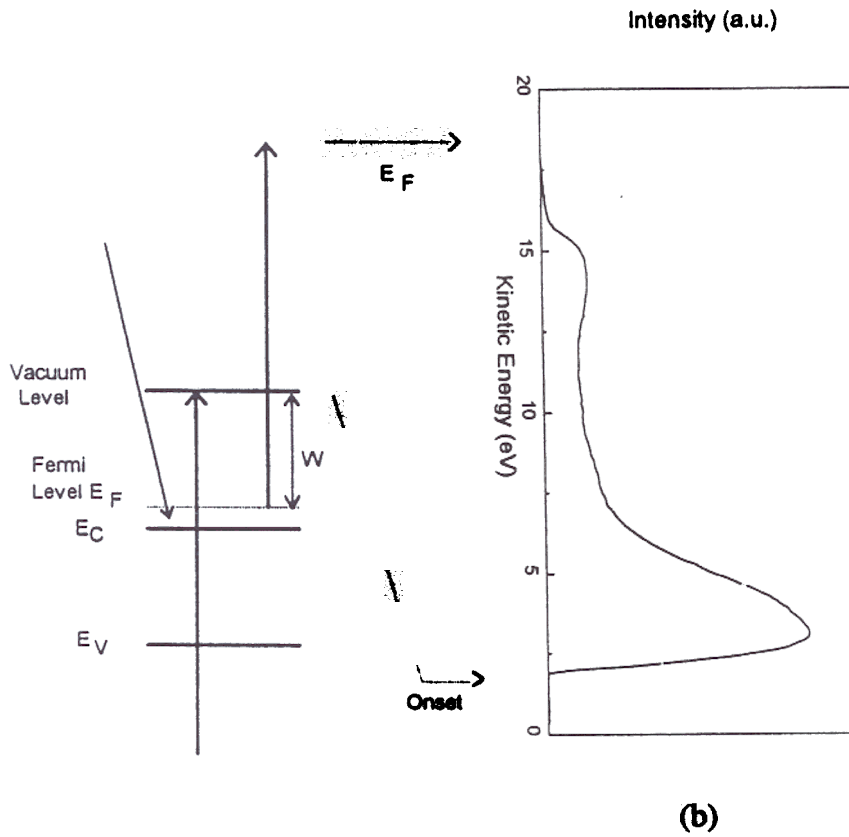
(b)

(c)

Fig. 5.10: UPS spectra of ITO treated in different ways: as-grown ITO, oxygen plasma treated (25W-open triangle, 150W-solid triangle), hydrogen plasma treated ITO (25W)

25W, 4 min. sample, and by ~0.3 eV in the 150W, 4 min. sample. The hydrogen plasma treatment reduces the work function by ~100 meV.

As introduced earlier, ITO is generally considered as a heavily doped and degenerate n-type semiconductor with both Sn dopants and structural defects such as the oxygen vacancies contributing to its conduction. However, the carrier concentration does not necessarily increase monotonically with the concentrations of the tin dopants or the oxygen vacancies [2,15-19]. For instance, in many previous publications, the carrier concentration and therefore the conductivity in ITO is highest at 4-6 at.% Sn, and drops at higher Sn concentrations [2, 15-18]. Without knowing the free carrier concentration near or at the surface, it is hard to determine whether the shift of the ITO surface work function is only due to the change in the concentrations of the tin dopants or the oxygen vacancies. Other phenomena could also result in the change of the ITO surface work function. A thin dipole layer might form at the surface during the exposure to the plasma and change the surface work function. For instance, the ITO(+)-O⁻ dipoles might form at the ITO surface during the oxygen plasma treatment and increase the ITO surface work function. Further, the band bending near the surface due to surface states or "traps", which might be produced by plasmas, is another possible cause for the work function shift. Such complications might explain why the ITO surface with the highest work function (oxygen plasma, 150W, 4 min.) does not give the best performance.

The AES analysis also points out the presence of carbon on the surface of the cleaned as-grown ITO. The removal of the organic residue from the ITO surface could therefore also be partially responsible for the device improvement. The inert Ar plasma does not seem to chemically affect the ITO surface. The slight improvement in devices made on Ar plasma-treated ITO could be due to a surface cleaning effect of Ar plasma or to residual oxygen in the RIE from venting to air for sample loading.

All the preceding discussions are based on the results from the characterization of the ITO surfaces before the organic layers are deposited. In the realistic situation, the

reaction or chemistry between the organic layer and the ITO surface may result into very different interface properties for differently treated ITO surfaces. Without further evidence and analysis, we are not sure what chemistry may be involved between the doped PVK layer and different ITO surface. However, we noticed that the ITO surface became more hydrophilic after the oxygen plasma treatment. The hydrophilicity of a surface is usually associated with the existence of hydroxyl (-OH) groups. The oxygen plasma treatment may make the ITO surface highly reactive so that it reacts with water in the air instantaneously to give a hydroxylated surface on removing the sample from the plasma reactor to the air. The hydroxyl groups can bond to the PVK via the hydrogen bond with the nitrogen atom on the carbazole group. This bond may not be conductive, but it may hold the carbazole group closer to the surface and help to form a more intimate contact between the doped polymer layer and the ITO. Such a more intimate contact may facilitate hole injection and improve the device performance. The above is just an example of possible surface chemistry between the ITO and the organic layer. Further exploration of the role of surface chemistry in the formation of ITO-organic interface definitely would be an interesting and useful topic for future work. Through the understanding of this surface chemistry, one may further manipulate it to improve device performance. This has actually been demonstrated recently [20]. It is found that a very thin layer (nearly a monolayer) of LiF deposited onto the ITO surface leads to improvements in operating voltage and quantum efficiency.

5.2 Pt Anode Contact

In addition to ITO, the high work-function metal Pt has also been tried as the anode contact to the single-layer doped polymer LEDs. Pt is deposited by e-beam evaporation at a rate between 1-2 Å/second with the base pressure of ~10^{-6} Torr and the

deposition pressure of $1\text{-}2\times10^{-5}$ Torr. The Pt is used either as deposited or is treated with the oxygen plasma prior to the spin-coating of the organic layer.

Fig. 5.11 shows the I-V and L-I characteristics of the OLEDs with the structure of Pt (350 Å)/PVK:PBD:C6 (100:40:0.3; 1400 Å)/Mg:Ag (1200 Å)/Ag (800 Å) in comparison with otherwise the same device using ITO as the anode contact. As in the case of ITO, the oxygen plasma also improves the Pt anode contact, reducing the drive voltage and raising the EL efficiency from ~0.1% to 0.2%. Since there is no similarity in the compositions of Pt and ITO and platinum is not easily subject to oxidization, it is hard to believe that the improvement is from the modification of the surface composition, as one of the possible reasons in the case of ITO. Instead, the generality of this phenomenon might suggest some common mechanism, such as the formation of a thin dipole layer at the anode surface (e.g. ITO(+)-O⁻ and Pt⁺-O⁻ dipoles at the ITO and the Pt surface).

The I-V characteristics of devices using oxygen plasma-treated Pt and ITO anode contacts are nearly the same, indicating that Pt is as efficient as ITO for hole injection into the organic layer. The EL efficiency of the Pt device is 0.2%, lower than 1% of the ITO device, because the 350Å thick Pt is semitransparent. This efficiency is still surprisingly high, considering the measured transmittance of the Pt is only ~6% within the EL spectral range of the organic layer. Since Pt is rather reflective (~60%) for visible light [21] and Mg:Ag/Ag cathode is a good mirror, the Pt/organic/Mg:Ag forms a "resonant cavity", i.e. "microcavity" for the light. The higher efficiency than expected might be from microcavity effects, which have been the topic of many OLED publications [22-24].

5.3 Cathode Contacts

In Fig. 5.12, the I-V and L-I characteristics of PVK:PBD:C6 (100:40:0.3 by wt., 1050 Å) devices using Mg:Ag/Ag, Ag, Au, and Al as cathode contacts are shown. The
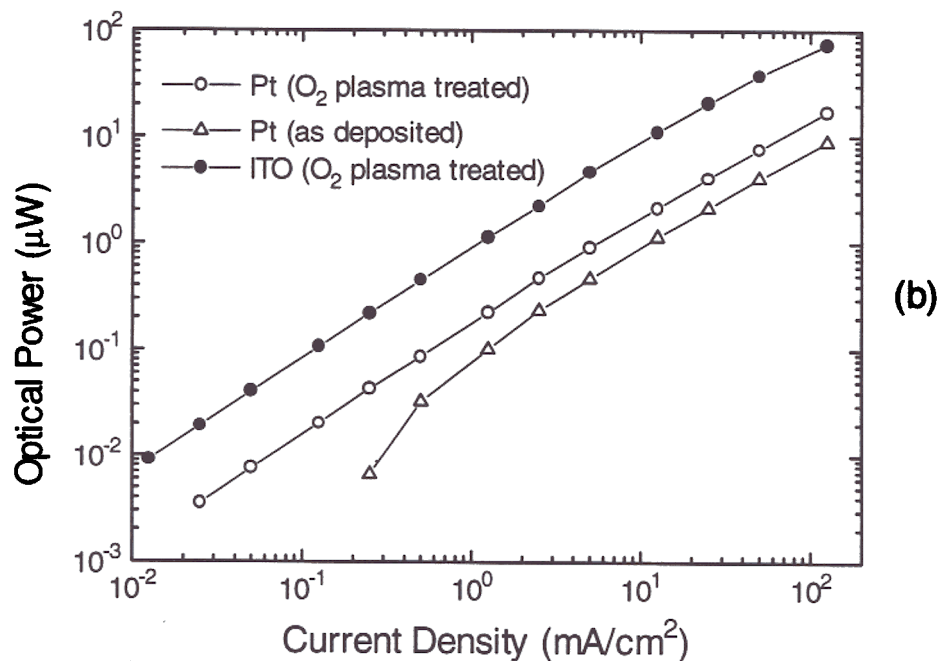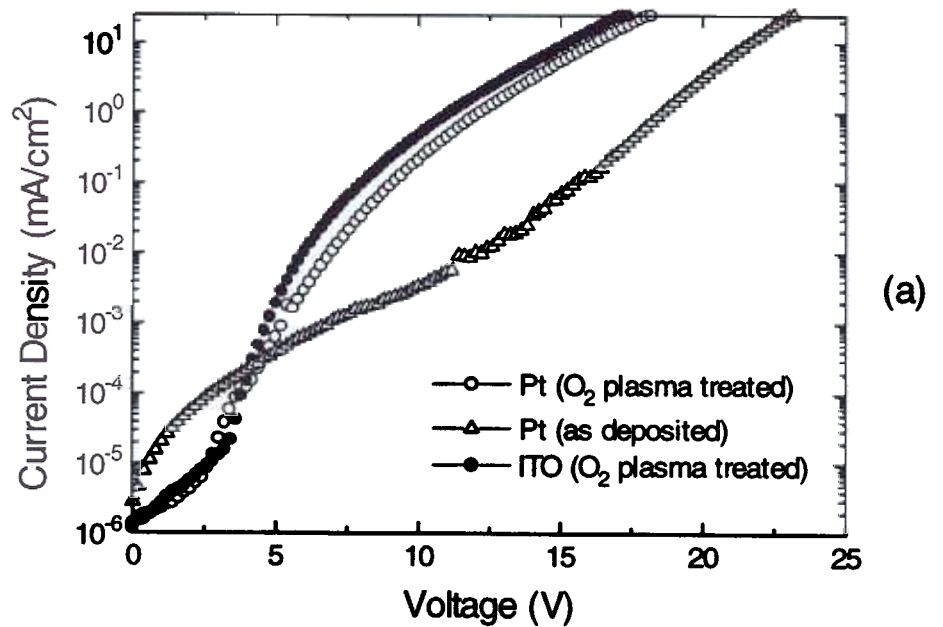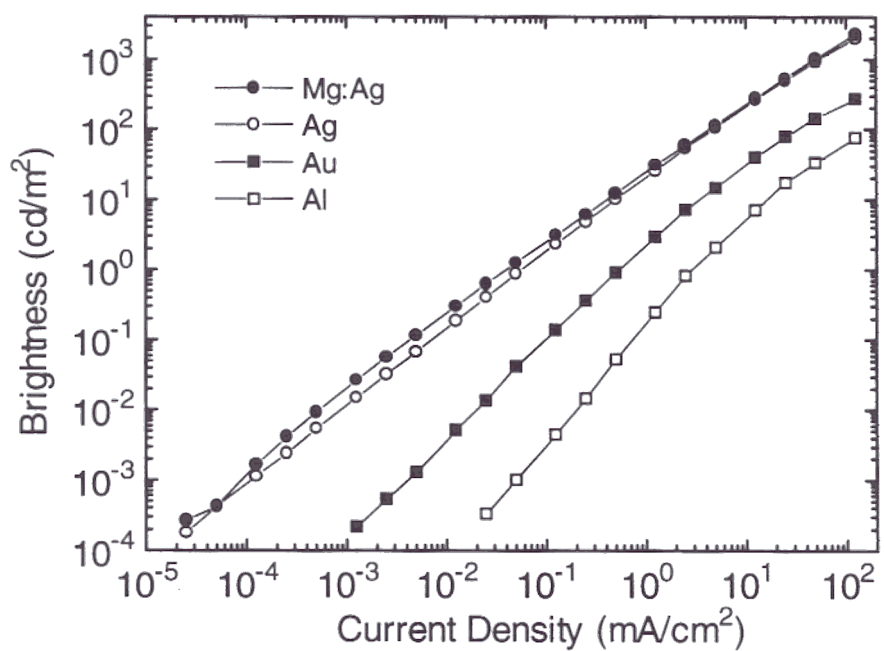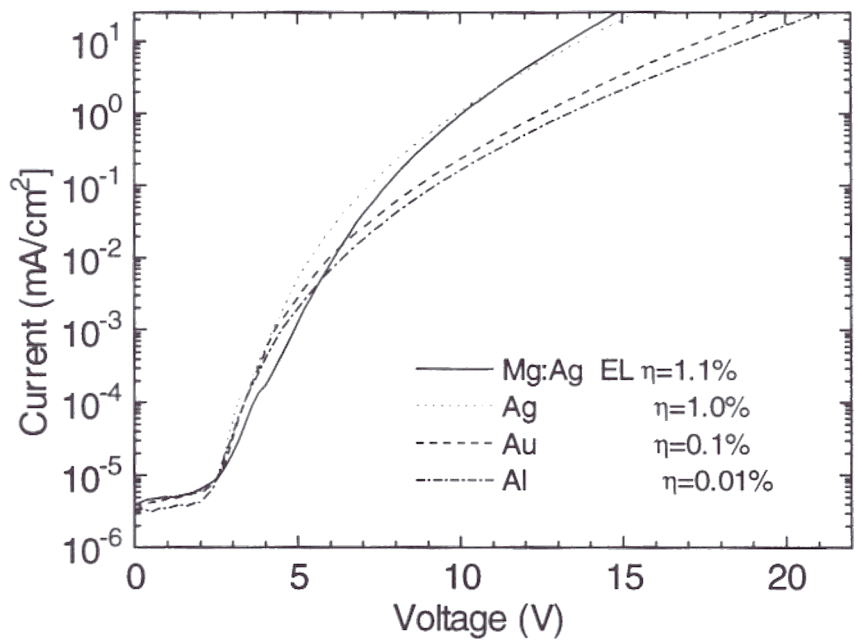
139

(a)

(b)

Fig. 5.11: I-V and L-I characteristics of the OLEDs with the structure of Pt (350 Å)/PVK:PBD:C6 (100:40:0.3; 1400 Å)/Mg:Ag (1200 Å)/Ag (800 Å), in comparison with the ITO device. Oxygen plasma: 150 mtorr, 25 sccm, 25 W, 4 min. Device area = 4mm^2.

Fig. 5.12: (a) I-V and (b) L-I characteristics of ITO/PVK:PBD:C6 (100:40:0.3 by wt.,
1050 Å)/Metal devices using Mg:Ag/Ag, Ag, Au, and Al as cathode contacts.

external EL efficiencies are 1.1%, 1.0%, 0.1% and 0.01% (at $5mA/cm^2$) for Mg:Ag/Ag, Ag, Au, and Al devices, respectively   Several features are observed in these I-V characteristics. First, the onset of the forward "bipolar" regime, around 2.5-3 V, is the same for all these metal cathodes in spite of the huge variation of EL efficiency. appears to be a feature of the organic/ITO (anode) contact and is independent of cathode contacts.   At higher current levels (> 0.01 mA/cm^2), there is an inverse relationship between the voltage and EL efficiency   For the same voltage, the drop of EL efficiency comes along with the drop of current   Since the only variable is the cathode metal, one concludes that a change in electron injection is the cause for both effects.   Poorer electron injection leads to imbalance of hole and electron currents and reduction of space-charge neutralization, which then result in poorer EL efficiency and higher   drive voltage also clear that in efficient devices, i.e. devices using Mg:Ag and Ag contacts, the hole current is not dominant, otherwise the change of electron injection and electron current should not substantially affect the total current.   Therefore, with a proper choice of cathode, the blend films have bipolar injection and transport abilities, as expected noticed that in the Au and Al devices, the brightness vs. current apparently deviates from the linear relationship, with the biggest deviation observed in the least efficient Al devices. In these devices, the hole current is probably dominant and the light output is governed by the presence of the electrons, which is injection limited.

There is no apparent trend for EL efficiency with the work functions of these metals, which are 3.7 eV, 4.3 eV (4.1-4.4 eV), 4.3 eV (4.2-4.7 eV), 5.1 eV (5.1-5.5 eV) for Mg, Al, Ag and Au, respectively [21]   The lack of an obvious correlation between device performance and metal work function implies an influence of the organic/metal interface, which strongly depends on the chemical properties and structures of the interface between an organic material and a particular metal, not a general dependence on work function   Although in the earlier development of OLEDs, it was found easier to make efficient OLEDs with cathodes involving reactive low work function metals [25-27],

142

there have been several recent reports of successful "interface engineering", in which the manipulation of the organic/metal interface allows the use of air-stable metals such as Al to fabricate even more efficient and low-voltage devices [28,29]. Despite the technological advancement, the characteristics of the organic/metal interface in OLEDs are in general not clearly clarified yet. In the present case, we found that air-stable Ag works nearly as well as reactive Mg:Ag alloy for this organic blend in terms of I-V characteristics and EL efficiency, in spite of the large difference in work functions, 4.3 eV of Ag vs. 3.7 eV of Mg. This may be related to the presence of oxadiazoles because there were some similar observations in previous publications [30-32], in which Ca and In cathodes gave similar device performance when electron-transport oxadiazoles were added into luminescent polymers.

5.4 Effect of Metal Coverage on Photoluminescence

There are always concerns regarding the effects of dielectric or metal coatings on the luminescence of organic thin films. In this section, the effects of different metal coverage on the luminescence of organic blend thin films are discussed. The setup for the PL measurement is shown in Fig. 5.13. Blend thin films of PVK:PBD:Bu-PPyV (100:100:2 wt., 110 nm) were coated on quartz or ITO/glass, with different metals deposited on top of the organic films. For each setup, there was one control sample without metal deposition. To ensure that the films are in the same optical environment, for the control sample without metal coverage, a metal (Al) coated glass mirror was used in physical contact with the organic film. It is assumed that the metal mirror placed adjacent to the polymer film is not the same as the deposited metal and that the deposited metal has intimate contact and the other does not. The PL spectra from films on quartz and on ITO/glass are displayed on Fig. 5.14(a) and Fig. 5.14(b), respectively. For both sets of samples, all the metal covered thin films have lower PL outputs than the control
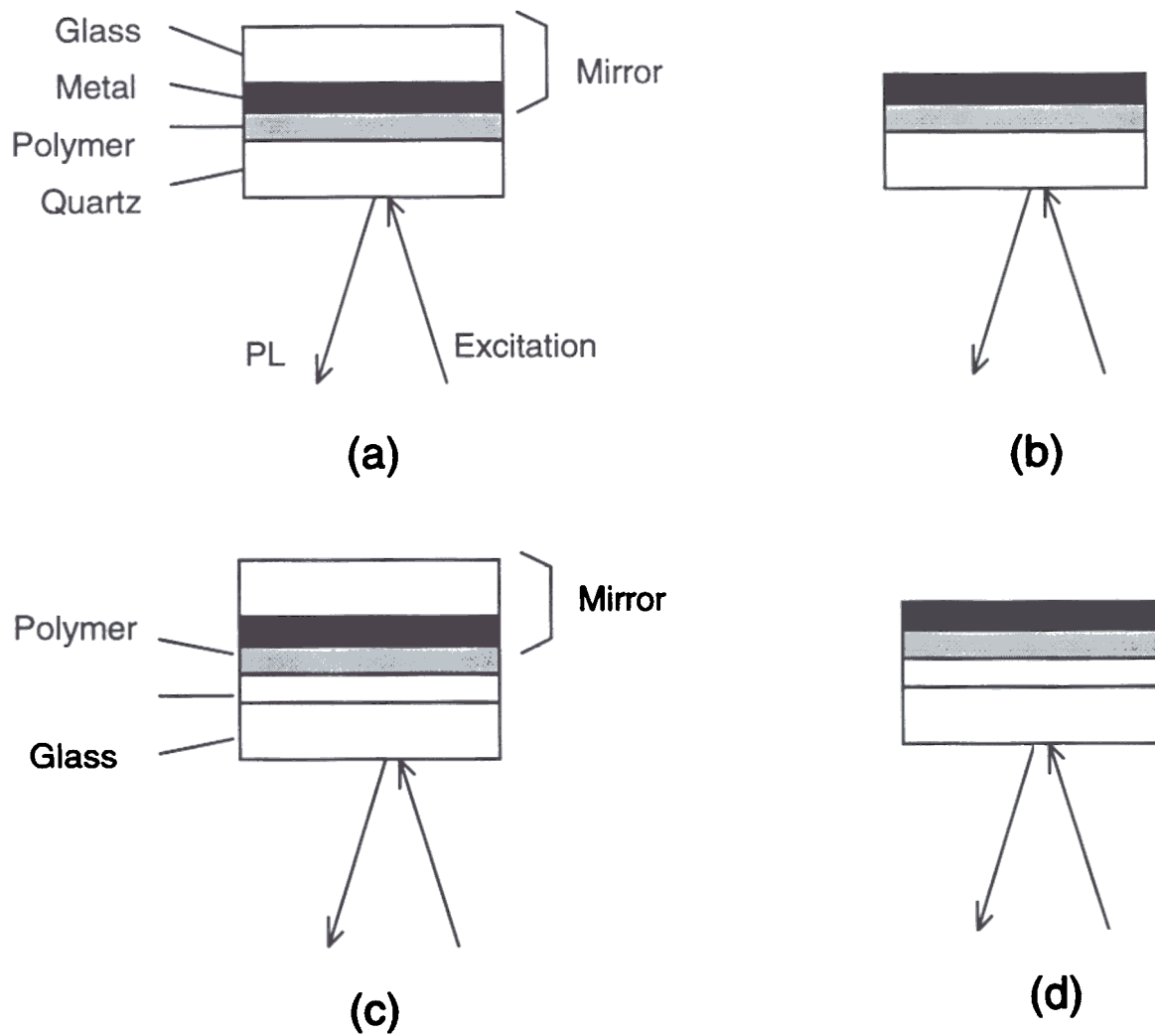
Fig. 5.13: PL measurement in various structures. (a) polymer thin film on quartz, in physical contact with an aluminum mirror. (b) polymer thin film on quartz, covered with a deposited metal layer. (c) polymer thin film on ITO, in physical contact with an aluminum mirror. (d) polymer thin film on ITO, covered with a deposited metal layer. The excitation wavelength is 340 nm.
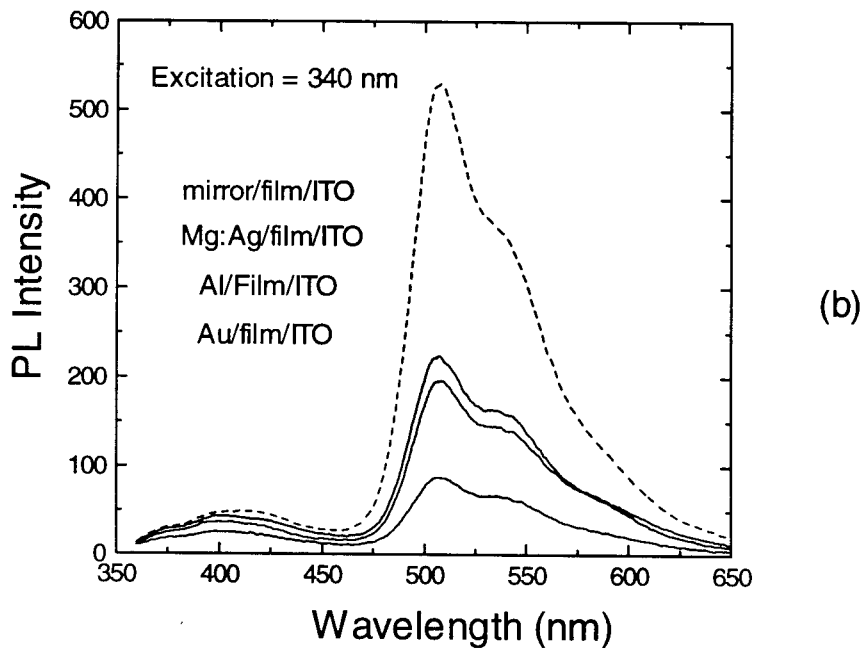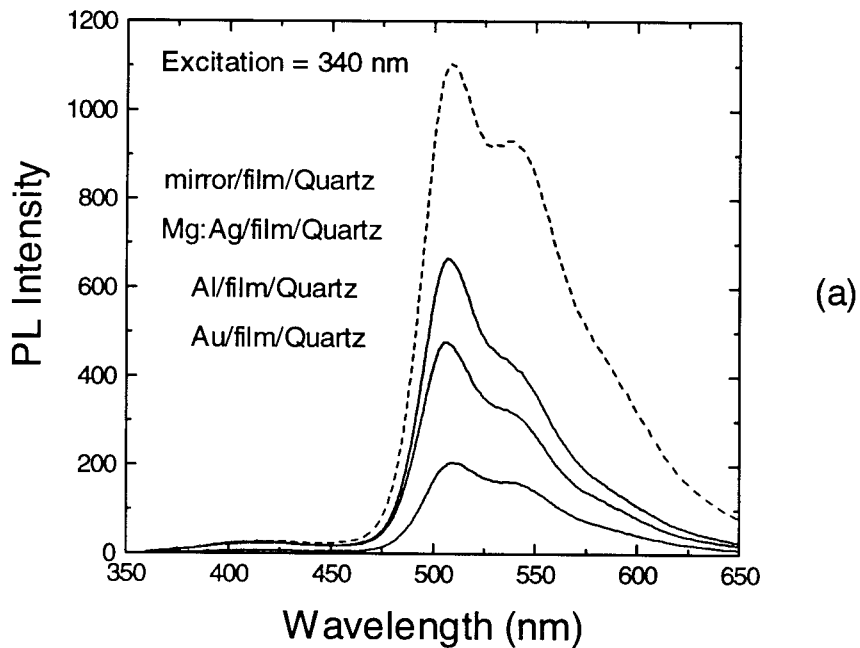
Fig. 5.14: (a) Measured PL intensity for structures (a) and (b) in **Fig. 5.13** with various metal coverages. (b) Measured PL intensity for structures (c) and (d) in **Fig. 5.13** with various metal coverages.

samples, apparently indicating that the metal films directly deposited onto the organic films do not just function as a mirror, like the metal mirror for the control sample. Furthermore, the luminescence intensity varies with deposited metal. There are several reports and proposed explanations for the effects of metal coverage on the luminescence of organic thin films [33-36]. One is the optical interference theory [34,36], in which the radiative lifetime (rate) of emitting species and the luminescence efficiency are dependent on the optical environment and the spacing between the emission zone and the interfaces. Also, metal overlayers on organic thin films could quench luminescence through several possible mechanisms [35,37,38]. First, energy level bending could cause field-induced luminescence quenching [37,38]. Also, interaction between metals and organics could produce products or interface states which would quench luminescence. Among the above, the contact quenching and energy level bending effects are particularly dependent on the metal deposited. From the device optimization point of view, a barrier/buffer layer with an appropriate carrier injection/transport ability on top of the blend thin film may be required to prevent carriers or excitons from recombining near the cathode metal contact or to control the spacing between the emission zone and the contact.

5.5 Summary

In summary, without degrading the bulk properties of ITO, the chemical composition of ITO surface layers could be substantially modified by treatment in plasma of different gases. As a result, the ITO anode contact to OLED and its device characteristics can be dramatically improved. Among all different treatments, an oxygen plasma is found to be the most effective in preparing the surface of ITO for high performance OLEDs. Such improvement is attributed to the change in work function due to the modification of the surface chemical composition or the formation of a thin dipole layer. In the OLEDs made from a PVK-based blend containing oxadiazoles, the